UNIVERSITY OF CALIFORNIA, SAN DIEGO

Testing the generalizability of basic receptive field models of retinal function

A dissertation submitted in partial satisfaction of the
requirements for the degree Doctor of Philosophy

in

Neurosciences with a specialization in Computational Neurosciences

by

Alexander Ken Heitman

Committee in charge:

Professor Donald I.A. MacLeod, Chair
Professor Ian S. Abramson
Professor Stuart Anstis
Professor Pamela Reinagel
Professor John Thomas Serences

2016

The Dissertation of Alexander Ken Heitman is approved, and it is acceptable in quality and form for publication on microfilm and electronically:

Chair

University of California, San Diego

2016

Table of Contents

List of Figures

Acknowledgments

I would like to first thank both my current advisor, Professor MacLeod, and my former advisor, Professor E.J. Chichilnisky, for their flexibility, support, and guidance over the past few years.

I would also like to thank all members of the Chichilnisky lab for their help, training and support. Dr. Martin Greschner in particular provided a large amount of guidance. Additionally I am also grateful for Dr. Alan Robinson for helping smooth the transition to psychophysics.

Chapter 1 presents the following manuscript in preparation for submission. Heitman, Alexander K.; Brackbill, Nora; Greschner, Martin; Sher, Alexander; Litke, Alan M.; Chichilnisky, E.J. "Testing pseudo-linear models of responses to natural scenes in the primate retina". The dissertation author was the primary researcher for the manuscript.

Chapter 3 presents the following manuscript in preparation for submission. Heitman, Alexander K.; MacLeod, Donald I.A. "Analyzing stimulus polarity configurations to examine neural factors underlying the Westheimer effect in peripheral vision". The dissertation author was the primary researcher for the manuscript.

Chapter 4 presents the following manuscript in preparation for submission. Greschner, Martin; Heitman, Alexander K.; Field, Greg D.; Li, Peter H.; Ahn, Daniel; Sher, Alexander; Litke, Alan M.; Chichilnisky, E.J. "Recurrent suppression in ON parasol retinal ganglion cells". The dissertation author conducted all of the modeling and simulation which generated two of the six figures in the paper.

I am grateful for all of the contributions from the co-authors.

Finally, I would like to thank my wife for her support throughout the entire process. Thank you.

Vita

2016	Ph.D. in Neurosciences with a specialization in Computational Neurosciences, University of California, San Diego
2011	M.S. in Mathematics, University of Utah
2008	B.S. in Mathematics, University of Pittsburgh
2008	B.A. in Economics, University of Pittsburgh

Abstract of the Dissertation

Testing the generalizability of basic receptive field models of retinal function

by

Alexander Ken Heitman

Doctor of Philosophy in Neurosciences with a specialization in Computational Neurosciences

University of California, San Diego, 2016

Professor Donald I.A. MacLeod, Chair

This dissertation consists of a series of findings which all demonstrate the inability of basic visual models to generalize to alternate conditions. In particular, this dissertation studies the receptive field of visual neurons, a concept well documented in the literature.

The first two chapters are concerned with linear cascade models of retinal ganglion cell function in the primate. These models start with a linear description of the receptive field and have had demonstrated success with artificial stimuli such as white noise. However, naturalistic stimuli represents a unique statistical regime and receptive field modeling schemes derived from artificial stimuli may not generalize. Utilizing population recordings

of the macaque ganglion cells to a novel naturalistic stimulus, this dissertation seeks to clarify and quantify the generalizability. Chapter one demonstrates that the key linear receptive field stage is an unsuitable approximation of the ganglion cell response when probed by naturalistic stimuli. Chapter two demonstrates that simple physiologically based modifications of the receptive field models are also inadequate. These two chapters both demonstrate and quantify the limits of generalizing the models to natural scenes.

Chapter three switches to human visual psychophysics but also addresses the question of generalizability. The chapter examines the Westheimer Effect, a well documented visual detection effect thought to be mediated by the classic center-surround receptive field of visual neurons. The effect has been primarily documented with a single polarity of visual stimulation, and the author seeks to test whether the underlying center-surround receptive field model is able to generalize to alternative polarities of visual stimulation. Again, the finding is that model generalizability is limited and alternative mechanisms beyond the original model are present.

Chapter four returns to the primate retina and explores an effect not generated by the classic receptive field. It is a peripheral effect which the authors relate to a novel amacrine interneuron. A basic receptive field model is then augmented with an amacrine mediated peripheral term to match the data. The basic receptive field model would have been insufficient to explain the observations.

Chapter 1

Primate retina ganglion cell response to naturalistic stimuli not explained by linear filtering

A central goal of systems neuroscience is to develop accurate quantitative models of how neural circuits process information. To describe retina function, simple models initiated by linear filtering of the visual stimulus have demonstrated repeated success in replicating gross features of the ganglion cell response across multiple species. However, these models have primarily been tested with artificial stimuli; therefore, the ability of linear filtering to capture the natural function of the retina remains uncertain. This paper presents a test of how accurately cascade models initiated by linear stimulus filtering explain the response to naturalistic visual stimuli in the primate retina. Light responses from macaque retinal ganglion cells were obtained using large-scale multi-electrode recordings, and two major cell types, ON and OFF parasol, were examined. Visual stimuli consisted of images of natural environments with simulated saccadic eye movements and fixational jitter. The generalized linear model (GLM), a cascade model which demonstrated high-fidelity response replication in the primate retina (Pillow2008 [15]), failed to replicate the recorded response to naturalistic stimuli. Fitting additional scalar nonlinearities before

and after the key linear filtering stage of the GLM did not correct these failures. These findings suggest that the function of the primate retina under natural conditions cannot be captured by models based in linear filtering. These findings highlights the potential importance of spatial nonlinearities, adaptive gain control, and peripheral effects.

1.1 Introduction

Decades of research on the retina have yielded many computational models of its function, starting with linear description of spatial receptive fields of retinal ganglion cells (RGCs) (Kuffler1953 [9]). A central goal of these computational models is to synthesize current understanding and provide quantitative predictions of responses to a range of visual stimuli. Modeling the RGC spiking response to spatio-temporal visual stimulation can be formally formulated as a mathematical transformation from a high dimensional vector space to a scalar non-negative series of discrete spiking events. The general consensus in the field has been to adopt simple cascade models where the initial step is to convolve the visual stimulus with a linear representation of the spatio-temporal receptive field. This initial linear filtering grossly simplifies the transformation by summarizing the cells interactions with the high-dimensional stimulus as a purely linear process. The subsequent portions of the cascade are largely a formatting process which generates a neural-like sequence of non-negative spiking events. Despite their simplicity, cascade models have robustly replicated the temporal structure of the light response to artificial laboratory stimuli (Keat2001 [8], Pillow2008 [15], Pillow2005 [14]). These results suggest that the ganglion cell response to visual stimuli can be summarized as being primarily linear.

However, responses to artificial stimuli may not reveal how the retina functions in the life of the organism. Naturalistic stimuli exhibit fundamentally different statistics from artificial laboratory stimuli, and numerous studies support the notion that the visual system is specifically tuned to represent natural scenes (Simoncelli2001 [24], Olshausen2004 [12], Pitkow2012 [16], Ratliff2010 [17]). Furthermore, diverse visual computations, including significant nonlinear summation within the receptive field, have been revealed in several

types of RGCs in several species, using tailored stimuli (e.g. Hochstein1976 [7], Enroth-Cugell1966 [5]). Nonlinear summation is inconsistent with models based in linear filtering, but it is uncertain whether the nonlinearities revealed with laboratory stimuli are relevant for retinal encoding of natural scenes (see Nirenberg2012 [11]). Given these diverse findings a fundamental question arises: can simple cascade models capture the responses of primate RGCs to naturalistic stimuli?

We address this question in the primate retina, the visual system which is most similar to that of humans and a species whose natural viewing is closest to that of humans. The specific cascade model we choose is the generalized linear model (GLM). The first key feature of the GLM is its ability to seamlessly incorporate spike conditioning. This enables the GLM to capture not only the precise temporal structure of light responses of individual RGCs, but also their concerted activity and thus in principle the full neural code (Figure 1.2) (Pillow2008 [15]). The second key feature of the GLM is the convexity of its parameter fitting function. Particularly for naturalistic stimuli and high parameter counts, it is pertinent to have a reliable and reproducible fitting scheme. Finally the GLM also permits optimal reconstruction of the stimulus from spike trains, which reveals how specific aspects of the neural response encode the stimulus (Bialek1991 [2], Rieke1997 [19]).

Here we test the ability of the GLM to account for primate RGC responses to natural images with simulated eye movements. Using large-scale multi-electrode recordings, we examined responses in populations of ON and OFF parasol cells, which initiate the magnocellular pathway of the primate visual system. The results indicate that the performance of the GLM in reproducing responses to naturalistic stimuli is markedly inferior to its performance with white noise stimuli (Figures 1.2, 1.3). We further demonstrate that a GLM modified with scalar nonlinearities before and after the linear filter (Figure 1.4) again is unable to reproduce the response to naturalistic stimuli with high fidelity. This finding in particular is highly suggestive that entire class of cascade models based in linear filtering is fundamentally insufficient for explaining RGC function in natural viewing conditions. Moreover, these findings highlight the necessity of building modeling schemes which go beyond the linear filtering by incorporating known neural properties such as nonlinear

computations, adaptation, or peripheral effects.

1.2 Results

Retinal ganglion cell responses to natural scenes

To understand the pattern of retinal responses elicited by natural scenes, large-scale multi-electrode recordings were obtained from retinal ganglion cells (RGCs) in the isolated primate retina. Spiking responses of complete populations of ON and OFF parasol RGCs were examined. Images of natural scenes from the van Hateren database (van-Hateren1998 [25]), were presented and jittered over time in a manner that simulated fixational eye movements, and were replaced once per second to emulate the rapid transitions that occur at saccades (see Methods 1.4, Figure 1.1A, B).

Natural scenes evoked patterns of neural response very different from those evoked by spatiotemporal white noise (Figure 1.1C). The combination of natural image structure and emulated eye movements produced strong and extended periods of firing and silence, compared to the more briskly but weakly modulated responses observed with white noise.

Testing the generalized linear model with natural scenes

To test whether the generalized linear model (GLM) can capture the responses to natural scenes, the model was first fitted to data obtained with white noise stimuli, and the fitted model was then used to predict light responses to both white noise and natural scenes (Pillow2008 [15]). In the GLM, the stimulus is first convolved with a spatiotemporal linear filter to produce a univariate generator signal over time. The generator signal drives spike generation through an exponential nonlinearity that controls the rate of an inhomogeneous Poisson point process (Figure 1.2A). These portions of the model are designed to capture the integration of light inputs over space and time, the nonlinear relation between stimulus strength and firing probability, and the stochastic nature of retinal responses. In addition, a fitted feedback waveform is added to the generator signal after each generated spike. This term permits the model to capture non-Poisson structure observed in real spike trains, such as refractoriness and bursting (Reich1998 [18], Berry1998 [1]). Finally, when several

neurons are being modeled, a fitted coupling waveform is also added after each occurrence of a spike in neighboring neurons, capturing interactions that are independent of the visual stimulus (Pillow2008 [15]) (not shown in Figure 1.2A).

Fits of the model parameters to white noise data revealed spatiotemporal filters and feedback signal structure similar to those seen in previous work (Figure 1.2B, 1.2F). With these fitted parameters, the GLM provided an accurate reproduction of the structure of RGC firing with repeated presentations of a new white noise stimulus, as expected (Figure 1.2C, 1.2G) (Pillow2008 [15]). However, this same model largely failed to reproduce the distinctive firing structure observed with natural scene stimuli (Figure 1.2D, 1.2H).

The inferiority of the model predictions with natural scenes compared to white noise was consistent in 75 ON and 181 OFF parasol cells examined across three retinas (Figure 1.2E). To summarize model performance across many cells, the quality of the model predictions was quantified in two ways (see Methods 1.4) that allow for the fact that firing structure is very different in the two stimulus conditions. First, the *fractional likelihood increment* was examined. This was defined as the log likelihood of the model predictions, minus the log likelihood that would be predicted by random firing, divided by the log likelihood of an optimal conditioned model (OCM) also expressed as an increment from random firing log likelihood. The OCM was a model in which the firing rate over time was determined by the measured average response time course to repeated stimuli, along with fitted feedback and tonic drive terms like those used in the GLM. The fractional likelihood increment provided a unitless measure of model performance approximately in the range $[0, 1]$, summarizing how accurately the model predicts the drive produced by the stimulus. Second, the *fraction of explainable variance* was examined, i.e. the degree to which the model captured the firing rate modulations that were reproducible across trials. This measure is also unitless and approximately constrained to the range $[0, 1]$.

Using both measures, model prediction accuracy was substantially lower for natural scenes stimuli than for white noise stimuli (Figure 1.2E). Note that the absolute model performance was different in the three retinas recorded, presumably due to differences in the preparations, including the degree of photopigment bleaching, receptive field sizes, and

other sources of variability between animals and experimental preparations. Thus, a GLM fitted to white noise data cannot explain light responses with natural stimuli, i.e. the GLM fails to generalize across viewing conditions.

Testing the adequacy of generalized linear model structure

One reason for the failure of the GLM to generalize, despite capturing responses to white noise accurately, could be that retinal processing adjusts to the statistics of the stimulus by changing properties of light response. Adaptive changes of this kind could potentially be captured by allowing for different parameters of the GLM in different stimulus conditions. If this were true, the GLM would remain useful for summarizing retinal responses, with the understanding that the model predictions are accurate only if its parameters are suitably adjusted to account for retinal adaptation to image statistics.

To test this possibility, the GLM was fitted to data obtained with a subset of natural scenes stimuli, and then used to predict the responses to a different subset of natural scenes. This approach produced more accurate predictions of light responses (Figure 1.3C, 1.3F). These improvements took the form of both minor corrections in the structure of the response as well as overall changes in gain tuning and tonic firing. However, the discrepancies between data and model remained large compared to those obtained with white noise (Figure 1.3D). Across three preparations, the results were consistent: fitting and testing the model with natural scenes produced substantially less accurate predictions of response than fitting and testing with white noise (Figure 1.3D). Thus, the parametric form of the GLM is less well-suited to capturing light responses with natural stimuli than with white noise.

Extensions of the model to capture simple nonlinearities

Although the GLM fails to capture natural scene responses, it remains possible that slight modifications to the model structure would improve its predictions and thus produce an accurate model with most of the technical and conceptual advantages of the GLM for understanding retinal function. A key simplifying feature of the GLM is the linear filter that integrates visual stimulus contrast over space and time to drive firing (Figure 1.2A) (Pillow2008 [15]). This is essential because it makes the model easy to interpret, and al-

lows for robust fitting as well as reconstruction of the stimulus from spike trains. However, many studies have revealed nonlinearities in retinal response that could underlie the observed failures of the GLM to reproduce responses to natural scenes (Hochstein1976 [7], Enroth-Cugell1966 [5]). To test the extensibility of the GLM, the model was augmented to accommodate scalar nonlinearities before and after the spatiotemporal integration step.

First, an instantaneous, point-wise nonlinearity was applied to the pixels of the stimulus after temporal integration expected from cone photoreceptors, but prior to the spatiotemporal filter in the model (see Methods 1.4; Figure 1.4A). This was performed by first convolving the stimulus over time with an estimated photoreceptor impulse response (see Methods 1.4) and then fitting the remaining model. This model structure would capture, for example, a nonlinear contrast-response relationship at the cone synapse prior to spatial and temporal processing in the retina. The power-law form of the nonlinearity,

$$f(x) = x^{\alpha}, \tag{1.1}$$

was fitted to the data by iteratively modifying the parameter (α) governing its shape, alternating with modifying the parameters of the rest of the model, to maximize likelihood. In three preparations, the form of the fitted nonlinearity was consistent for natural scenes, and consistent for white noise (Figure 1.4B, 1.4C, 1.4F, 1.4G), but different for the two types of stimuli. Thus, the modified model apparently captured systematic departures from linearity early in the retinal circuitry. However, this modified model produced only a marginal improvement in prediction of light responses.

Second, the exponential nonlinearity in the GLM was modified to allow for different nonlinear transformations of the generator signal controlling firing probability. This model structure would capture, for example, a synaptic transfer between bipolar cells and RGCs that saturates for strong stimuli. The nonlinearity,

$$f(x) = \frac{\alpha}{(1 + \exp(-\beta x))}, \tag{1.2}$$

was again fitted by iteratively adjusting the parameters (α, β) governing its shape, alter-

nating with the GLM parameters. This procedure resulted in reproducible fits with a consistent form across data sets (Figure 1.4B, 1.4C, 1.4F, 1.4G). Again, however, this manipulation did not change the relationship between white noise and natural scene predictions.

Finally, the results of fitting both simple nonlinearities was tested. The results (Figure 1.4E) indicate that the model continues to produce substantially less accurate predictions with natural scenes compared to white noise. Simulated rasters showed minor improvement from the standard GLM but still featured major errors (Figure 1.4D, 1.4H). In summary, allowing for simple nonlinearities both before and after spatiotemporal integration in the model produced evidence of systematic nonlinear behavior not captured by the original GLM, but did not allow the model to capture responses to natural scene with substantially higher accuracy. Moreover the structure of the likelihood metric (see Methods 1.4), incorporates inaccuracies which could be attributable to the post-spike filter. The failure of the modified GLM to capture the response to naturalistic stimuli is thus likely to be attributable to the linear filtering of the stimulus.

Impact of coupling on response prediction

A powerful feature of the GLM, not incorporated in the analysis above, is that it can capture the cross-correlation in firing between RGCs that is independent of the visual stimulus, using coupling term with a structure similar to the internal feedback term in the model (Figure 1.2A). In previous work, coupling had little effect on the average light response of a given cell to white noise; instead, it primarily helped account for trial-to-trial response variability (Pillow2008 [15]). Nonetheless, to test whether coupling could affect the performance of the GLM with natural scenes, model predictions were examined with a coupled model.

Specifically, a subset of cells was examined in which all the immediate neighboring cells of the same type were recorded, providing a nearly complete measurement of local interactions (Shlens2006 [22], Shlens2008 [23]). Testing a coupled model with natural scenes requires taking into account the effects of a stimulus with strong spatial correlations. These correlations have the potential to confound the analysis, by causing the response of the cell

being modeled to be predicted accurately using the spikes observed in neighboring cells, rather than by accurately capturing how well the stimulus drives the cell being modeled.

To account for the potential confounds, a blind coupling model (BCM) was constructed and used to normalize the measure of performance. The BCM consists of a tonic drive term and a full set of coupling filters to all adjacent ON and OFF parasol cells (see Pillow2008 [15] for details). The BCM lacks a stimulus filter for the modeled cell; its purpose is to provide a measure of how stimulus induced spike correlations can drive prediction accuracy in a coupled model. The GLM with coupling was then assessed by calculating its improvement over the performance of the BCM, instead of the OCM normalization used for analysis of single cells (Figure 1.2 – 1.4). For all cells and both metrics, the GLM with coupling exhibited more accurate predictions with white noise than with natural scenes; that is, the addition of coupling did not affect the main conclusions about the performance of the GLM in these conditions.

1.3 Discussion

The present results show that the generalized linear model (GLM), which successfully captures the responses of populations of primate retinal ganglion cells (RGCs) to white noise stimuli, fails to capture responses as accurately with natural scenes stimuli (Figure 1.2). This failure not only reflects the inability of the model parameters to generalize across stimuli with different statistics, but also reflects structural deficits in the model (Figure 1.3). Furthermore, simple nonlinearities added to the model to account for known retinal mechanisms had little effect on the conclusions (Figure 1.4), nor did the addition of coupling between cells. The results suggest that models with fundamentally nonlinear structure, potentially including subunits and adaptation, will be necessary to capture how the primate retina represents the visual environment for which it evolved.

Comparison to expected results from previous synthetic models

Since the first experiments demonstrating the center-surround properties of RGCs, many studies have explored the neural computations in the retina which produce the pat-

terns of neural activity transmitted to the brain. Broadly, two categories of models have emerged: (1) *synthetic* models with primarily linear properties, that can be readily interpreted, fitted to diverse experimental data, and used to succinctly summarize visual computations across a range of conditions (see Chichilnisky2001 [3]), and (2) *specific* models, usually designed to capture results of a particular visual stimulus manipulation, which provide insight into computations and mechanisms in the retina but are generally less broadly useful for a fuller description of the full retinal output signal.

The GLM is an instance of a synthetic model – essentially linear, but with simple nonlinear components and conditioning terms added to account for major features of RGC response not captured by simpler models (nonlinear dependence on stimulus strength, non-Poisson time structure such as bursting and refractoriness, and concerted firing across cells). The structure of the GLM allows it to capture a wide variety of response patterns elicited by white noise stimuli, in complete populations of neurons, with striking accuracy (Pillow2008 [15]). Given its mostly linear structure, however, it is not surprising that substantial failures of the GLM can be observed in some conditions (e.g. Figure 1.2D, 1.2H) (e.g. Hochstein1976 [7]). It is also not surprising that these failures are larger with natural scenes than with white noise (e.g. Figure 1.2C, D, G, H), because white noise only modestly modulates RGC firing and thus may keep responses in a more linear operating range, while natural scenes produce large changes in firing during and between presentation of distinct images. In this sense, the results presented here serve mainly to confirm expectations.

However, previous work also suggests that the results could have been quite different. Some studies point to nearly linear signaling in RGCs of some types in some species (Enroth-Cugell1966 [5]), with nonlinearities primarily observed with targeted artificial stimuli. It is unclear how important these nonlinearities would be for encoding of natural scenes by the retina. Furthermore, previous strictly linear models failed to account for important features of light responses that are captured by the GLM, such as accelerating response to increasing stimulus contrast, and non-Poisson spike train structure. Therefore, one might expect the GLM to capture a greater range of retinal responses than the strictly linear models used in previous work. Furthermore, recent work suggested that pseudo-linear

models similar to the GLM can capture aspects of RGC responses in the mouse retina to natural scenes (Nirenberg2012 [11]), although the coarse analysis of response structure compared to other recent studies with similar models (Chichilnisky2001 [3], Keat2001 [8], Pillow2005 [14], Pillow2008 [15]) leaves the findings open to different interpretation. Finally, recent findings in primate parasol RGCs reveal changes in the degree of response linearity with light level using artificial stimuli (Schwartz2012 [20]).

Thus, the findings reported here were necessary to clarify and quantify whether a synthetic model with proven success could capture natural light responses in populations of RGCs, in the retina most similar to that of humans. Compared to its performance with white noise stimuli, the performance of the GLM falls short with natural scenes stimuli (Figure 1.2), and this failure reflects not only the need to change parameters across stimulus conditions, but a structural inability of the model to capture responses to such stimuli (Figure 1.3).

Simple extensions of the generalized linear model

The utility of synthetic models like the GLM is in their capacity to predict the function of the neural circuitry being modeled, as opposed to reflecting all its component parts. In principle, more complex models that capture retinal mechanisms in greater detail would out-perform a simple synthetic model like the GLM (e.g. Schwartz2012 [20]). However, such models typically greatly increase the complexity of the fitting process, particularly with non-symmetric stimuli such as natural scenes, and the amount of data necessary to constrain the parameters. An alternative approach is to augment a synthetic model with simple components that can capture a greater range of responses. An example is the linear-nonlinear-poisson cascade model (see Chichilnisky2001 [3]) which extended purely linear models to account for the accelerating response to stimulus contrast, but is nearly as tractable and interpretable as purely linear models.

The addition of scalar nonlinearities before and after the key spatiotemporal linear step of the GLM (Figure 1.4) provided an opportunity to improve its predictive power, without substantially increasing the complexity of the model or the fitting procedure. Specifically, a scalar nonlinearity adds only a small number of parameters, and these can

be fitted to data by alternating the relatively simple adjustment of the new parameters with the adjustment of the more numerous GLM parameters that, in isolation, are guaranteed to converge to a global optimum (Paninski2004 [13]). If the addition of the pre-filtering and post-filtering scalar nonlinearities had substantially improved model predictions for natural scenes, they would have constituted a worthwhile increment in complexity in the interest of predictive power. However, this was not the case (Figure 1.4).

Implications for future work

The present results reveal that neither the GLM nor simple variants of it will capture responses to natural scenes in the primate retina with the fidelity that the GLM exhibited in capturing responses to white noise. This strongly suggests that at least some of the phenomena and mechanisms revealed in many experiments with artificial stimuli will be necessary to explain the output of the retina in natural viewing conditions. Important examples include nonlinear subunits within the receptive field (Hoschstein1976 [7]) and adaptation to stimulus intensity and variance. Future efforts will be needed to determine which aspects of retinal circuitry are essential for understanding its natural function.

1.4 Methods

Recordings

Preparation and recording methods are described elsewhere (Chichilnisky2002 [4]; Frechette2005 [6]; Litke2004 [14]). Briefly, eyes were enucleated from three terminally anesthetized macaque monkeys (Macaca sp.) used by other experimenters in accordance with institutional guidelines for the care and use of animals. Immediately after enucleation, the anterior portion of the eye and the vitreous were removed in room light. Segments of peripheral retina (red dots $5mm$, green dots $11mm$, blue dots $12mm$) were dissected and placed flat, RGC side down, on a planar array of extracellular microelectrodes. The arrays consisted of 512 electrodes in an isosceles triangular lattice. For one retina (red dots), the array had $30\,\mu m$ spacing, covering a hexagonal region with $450\,\mu m$ on a side; for the other two retinas (green and blue dots) the array had $60\,\mu m$ spacing covering a

rectangular region of $1800\,\mu m$ by $900\,\mu m$. While recording, the retina was perfused with Ames' solution ($33-34°C$) bubbled with 95% O_2 and 5% CO_2, pH 7.4. Voltage signals on each electrode were bandpass filtered, amplified, and digitized at $20\,kHz$. A standard spike-sorting algorithm was followed and only spike clusters which preserved a one millisecond refractory period and possessed physiologically plausible electrical image structures were defined as cells (Litke2004 [14]).

Visual stimulation

Visual stimuli were delivered using the optically reduced image of a CRT monitor refreshing at $120\,Hz$. The optical path passed through the ganglion cell layer and was focused on the photoreceptor outer segments. The emission spectrum of each display primary was measured with a spectroradiometer (PR-701, PhotoResearch) after passing through the optical elements between the display and the retina. The power of each display primary was measured with a calibrated photodiode (UDT Instruments). The mean photoisomerization rates for the L, M, and S cones were estimated by computing the inner product of the power scaled emission spectra per unit area with the spectral sensitivity of each opsin and multiplying by the effective collecting area of primate cones ($0.6\,\mu m^2$) (Professor Rieke Personal Communications). During colored and achromatic white noise stimulation, the mean background illumination level resulted in photoisomerization rates of $(4100, 3900, 1600)$ for the (L,M,S) cones. The naturalistic stimulus results in mean photoisomerization rates of $(1900, 1800, 700)$ for the (L,M,S) cones.

Cell type classification and Receptive Field Estimation

Cell types were identified by analyzing the spatiotemporal spike triggered average of the cells response via reverse correlation to a colored flickering noise stimulus (Litke2004 [14]). All subsequent modeling and analysis was restricted to the ON Parasol and OFF Parasol cells. Receptive fields were estimated by fitting a two-dimensional gaussian to the spatial component of the rank 1 projection of the spike triggered average. Subsequent analysis of each cell encompassed its entire receptive field by including at the minimum all pixels which were within two standard deviations of the center of the fitted gaussian.

Generalized Linear Model (GLM)

The basic GLM used in this paper consists of an initial linear spatiotemporal filtering of the visual input, followed by a scalar exponential nonlinearity controlling firing probability, followed by Poisson spike generation, which was then followed by a feedback signal summing with the post-filtered signal for each spike generated (Figure 1.2A). The linear filter and feedback waveform are fitted to maximize the likelihood of the fitting data given the model. Previous work showed that the GLM captures the responses of individual primate RGCs and complete populations of RGCs to white noise at least as accurately as any other model that has been tested (Pillow2008 [15]). The structure of the GLM (specifically, the likelihood function is log-convex in the model parameters) ensures that the model fits are uniquely and reliably estimated from data (Paninski2004 [13]). Moreover, it has been proven that the stimulus filters fit by the GLM are formally identical to what would be fitted under a maximally informative dimension paradigm (Sharpee2004 [21]), unifying the two disparate techniques with an approachable convex model (Williamson2015 [26]).

The fitted parameters of the GLM were organized as follows: a tonic rate term $(\mu, 1\,parameter)$, a spatio-temporal stimulus filter $(k, 199\,parameters)$, and a post-spike filter $(h, 20\,parameters)$. These parameters (μ, k, h) linearly combine with their respective time-varying covariates $(1,\ stimulus(t),\ spike_{history}(t))$ to produce a scalar generator signal which is binned at $1200\,hz$. The generator signal is then run through an exponential nonlinearity to produce a strictly positive firing rate $\lambda(t)$,

$$\lambda(t) = \exp(\mu + k * stimulus(t) + h * spike_{history}(t)). \tag{1.3}$$

The stimulus filter was constructed by computing the outer product of a spatial filter (169 spatial location parameters on a 13×13 grid) with a temporal filter (30 time sample parameters) and maps the high-dimensional spatio-temporal images to a scalar function of time. The spatial parameter grid was centered on the receptive field of the cell, estimated using reverse correlation to a distinct colored noise stimulus. The space filter was always large enough to comfortably capture the entire receptive field of each fitted cell. The time

filter captures the temporal integration properties of the cell and spans a 240 millisecond interval (with each of the 30 time filter parameter representing an 8-millisecond step of time). The output generator signal is effectively a running similarity score between 240 millisecond long sequences of stimulus and the stimulus filter and is hence both positive and negative. The generator signal is then added to a stimulus independent tonic firing term (μ) before being run through an exponential non-linearity to produce a strictly positive time-varying rate. Spikes are subsequently generated by a Poisson process binned at $1200\,hz$.

To add neural realism and correct for inherent flaws of a memory-less pure poisson process, a post-spike filter (h) is incorporated (Pillow2008 [15]). The post-spike filter is induced following each generated spike and describes the spike-induced gain change over the subsequent 100 milliseconds. The post-spike filter thus is a convenient way to incorporate spike history while still maintaining the simplistic cascade structure. A previously developed basis of raised sinusoidal humps (Pillow2008 [15]) was utilized to keep parameter count down to 20. The post-spike filter by its very construction inherently poses the threat of positive feedback which in-turn could generate physiologically implausible runaway spiking behavior. To prevent this, the model fitting routine was restricted to a subdomain where the temporally integrated spike-induced gain of the post-spike filter was kept below one.

All parameters (μ, k, h) were fit by maximizing an objective value which is monotonic to the likelihood of the fitting data given model parameters. The objective function is convex in parameter space, moreover the resulting gradient and hessian terms have explicit closed forms. This enables fast and reliable integration into automated optimization routines. Convexity is a key attribute when fitting high parameter counts to naturalistic stimuli which lack the symmetry of white noise.

Stimulus

The GLM was fitted to both a novel naturalistic stimulus, and to an achromatic binary white noise stimulus. The naturalistic stimulus consisted of 900 achromatic images from a standard database (vanHateren1998 [25]). Each image was flipped horizontally and vertically to obtain a total of 3600 unique images. The images were displayed on the

monitor for one second, and jittered over time according to measurements of fixational eye movements obtained from fixating, awake macaque monkeys (Z. M. Hafed and R. J. Krauzlis, personal communication).

Both stimuli were presented in sequences which interweaved the fitting stimulus with a cross validated test stimulus. For the naturalistic stimulus an additional set of 30 images were used to generate a 30 second test stimulus. The full fit and raster sequence consisted of 60 iterations of 60 seconds of novel fitting stimulus followed by the 30 second test stimulus. The naturalistic stimulus sequence thus resulted in one hour of model fitting interwoven with 60 repeats of a 30 second cross-validated test raster. The white noise stimulus was presented in a similar manner and resulted in 30 minutes of model fitting interwoven with 60 repeats of a 10 second cross-validated test raster.

Cell-Selection Criterion:

In order to guarantee that model failures are attributable to the model rather than poor fitting, all ON Parasols and OFF Parasols were subject to a convergence criterion cut. To be selected a cell's objective value fit must have converged 90% in half of the fitting time. This cut dropped the cell count from 495 cells down to 299 cells.

$$CUT1 : Improvement(50) \geq .9 * Improvement(100).$$

$$Improvement(N) := objval(GLM\ fitted\, with\, N\%\, of\ data) - objval(static\, rate). \tag{1.4}$$

Additionally, to ensure a certain quality of raster repeats a second cut was made independent of model fitting. Raster repeats were split into odd and even trials. For a cell to qualify, the fraction of variance explained (FVE) from the odd to even trials must exceed 50% for both the white noise test raster as well as the naturalistic test raster. Of the original 495 cells 414 cells passed the cut. This dropped the final cell count for analysis from 299 cells down to 256 cells.

$$CUT2 : FVE(rate_{oddraster}(t),\, rate_{evenraster}(t)) \geq .5$$

$$FVE(r(t), s(t)) := \int (r(t) - s(t))^2\, dt \div \int (s(t) - \overline{s})^2\, dt \tag{1.5}$$

Evaluation Metrics

Fractional Likelihood Improvement (FLI) is a monotonic transform of likelihood and was derived to evaluate model performance in rasters of grossly different spiking structure. The base measure is Likelihood-Improvement (LI) which is well defined for any model and is computed over the cross-validated raster. (LI) measures the information present in the model which is not accounted for by knowing the average firing rate of the test raster and is proportionate to the bits-per-spike of the model (Williamson2015 [26])

$$LI(model) = \log(P(raster|model)) \; - \; \log(P(raster|static\,rate)). \tag{1.6}$$

Comparing LI alone fails to control for the inherently different quantities of information available in the white-noise and natural scenes as well as the inevitable difference in raster quality across preparations.

Therefore a novel normalizing model called the optimal conditioned model (OCM) was fit directly to the test raster to handle this challenge. The OCM represents a near-optimal spike conditioned rate model performance and consists of a time varying rate term, a post-spike filter, and a tonic rate term. The time varying rate term is derived by smoothing the raster spikes by gaussians (sigma of $10\,msec$), the post spike filter is also fit by the raster and utilizes the same basis functions as the GLM, finally an additional tonic drive term is added to counter-balance the effect of adding a post-spike filter. By construction, the OCM encapsulates the error in poisson spike generation and the post spike filter. It follows that OCM normalization renders GLM failures directly attributable to the stimulus to generator score transformation. The OCM also effectively handles preparation differences and is able to properly bound all (FLI) scores by one.

$$FLI(GLM) = LI(GLM) \,/\, LI(OCM) \tag{1.7}$$

(FLI) however does not test the model's ability to simulate and replicate the cross-validated rasters. Thus a straight-forward fraction of variance explained (FVE) was also used to provide a balanced account of model performance. For each cell, recorded and

simulated repeats were summed and convolved with 10 millisecond gaussians to produce a net recorded rate and a net simulated rate. The standard fraction of variance measure from linear regression analysis was applied to provide a first order description of similarity between recorded and simulated repeats.

However, fraction of variance alone does not account for how reproducible the raster is in the first place. Therefore a Fraction of Explainable Variance metric (A.U.) was constructed by normalizing the fraction of variance score. The normalizer is the fraction of variance score derived when splitting the repeat rasters into odd and even trials, essentially quantifying how well the raster predicts itself. This successfully bounds over 99% of the scores by 1.

$$FEV := FVE(rate_{GLM}(t),\, rate_{fullraster}(t)) \div FVE(rate_{oddraster}(t),\, rate_{evenraster}(t)) \tag{1.8}$$

Input Nonlinearity

The initial cone transduction process is known to be nonlinear and a pointwise nonlinearity was fit to take into account this reality. The original stimulus was first run through a temporal kernel which was derived from a linear estimate of the cone signal. Following the temporal kernel, the stimulus was rescaled to $[0, 1]$ and then underwent a uniform point-by-point power-raise to each stimulus pixel.

$$f(x) = x^p \tag{1.9}$$

This parametrization allows for smooth monotonic reshaping which preserves the end-points and enables exploration of varying degrees of accelerating and compressive nonlinearities. An iterated fit approach with three repeats of GLM optimization followed by non-linearity optimization was utilized.

Output Nonlinearity

Another plausible explanation for the failure to replicate natural scenes is that

the exponential function is the "wrong" description of the transformation from stimulus filter output to firing rate. To remedy this the exponential was replaced with a two parameter logistic with parameters optimized by likelihood maximization. Logistic fitting was interwoven with refitting of the tonic drive and post-spike filter terms to compensate for changes in firing rate.

The full optimization consisted of three steps. First the input of the nonlinearity was defined to be the z-scored output of the linear stimulus filter. Second, the two parameters (L, r) of the logistic were fitted by likelihood maximization. Finally the post-spike filter and tonic drive terms of the GLM (μ, h). A second repeat of the iterated fitting was not necessary.

1.5 Figures

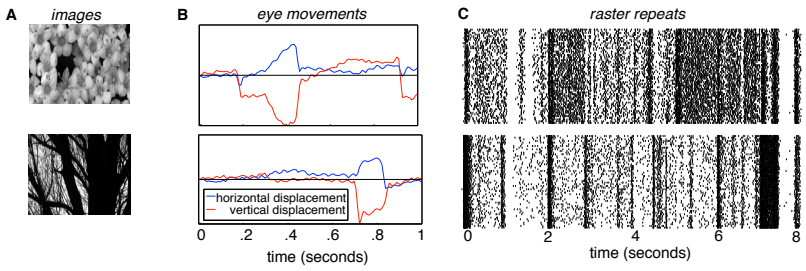

Figure 1.1: **Natural scene stimuli and responses**. **A.** Sample images taken from the van Hateren database (vanHateren1998 [25]). **B.** Two one-second fixational eye-movement traces taken from recordings of awake fixating macaques (see Methods 1.4). Note presence of microsaccades, drift and tremor. **C.** Sample of recorded rasters of response to a natural scenes stimulus (top: ON parasol, bottom: OFF parasol). Each tick represents the occurrence of a spike, each row represents a distinct repeated presentation of the stimulus (total of 55 trials). Note strong sustained periods of spiking and silence. See Figure 1.2 for comparison to white noise response.

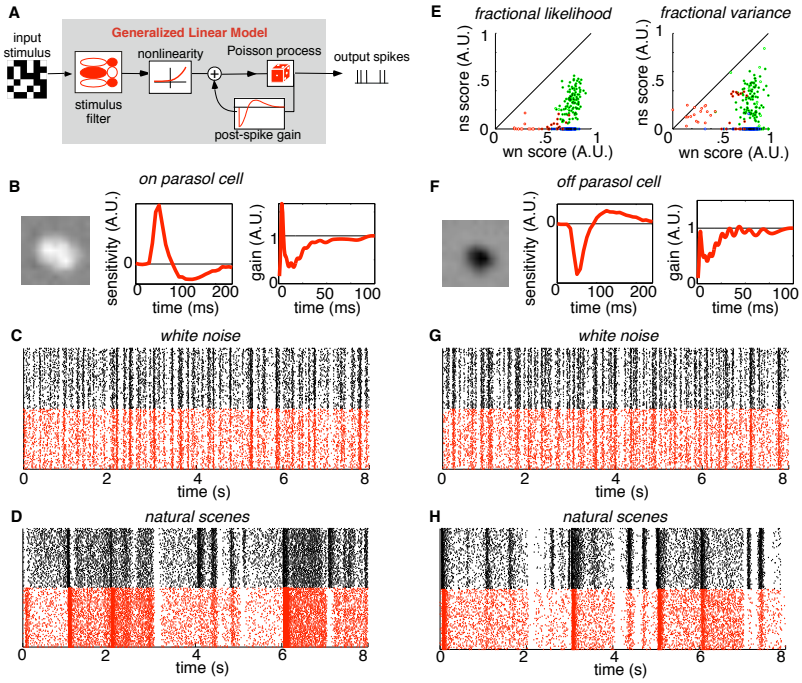

Figure 1.2: **Generalized linear model (GLM) fitted to white noise does not capture responses to natural scenes**. **A.** Schematic of GLM, with stimulus filter, response nonlinearity, stochastic spike generations, and post-spike feedback. See text for details. **B.** Sample GLM components obtained from fits to white noise data, for an ON parasol cell. The stimulus filter is decomposed into its separable spatial (left) and temporal (middle) components. The feedback filter (right) is expressed in terms of gain after the exponential nonlinearity (see Methods 1.4). **C.** White noise raster for same ON parasol cell (black, 55 repetitions). Response structure is approximately reproduced by the fitted model (red). **D.** Natural scenes rasters for the same ON parasol cell (black, 55 repetitions). Response structure is not reproduced by the white noise fitted GLM (red). **E.** Comparison of GLM predictions of responses to white noise (CG) and natural scenes (DH), using fractional likelihood (left) and fraction of explainable variance (right). In both cases the GLM was fitted to white noise data. See text for details. Colors of points denote different retinas. White-center points represent ON parasol cells, black-center points represent OFF parasol cells. **F-H.** Same as B-D for a sample OFF parasol cell.

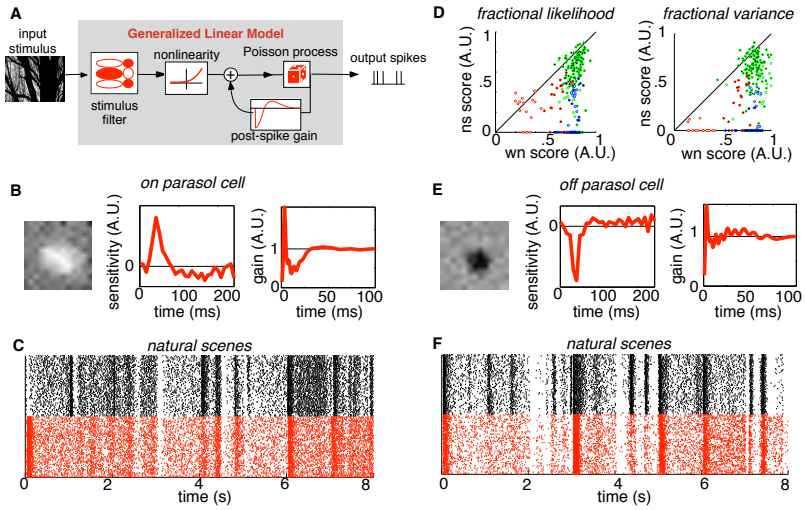

Figure 1.3: **GLM fitted to natural scenes data performs similarly**. See Figure 1.2 for comparison. **A.** Schematic of the GLM, fitted with natural scenes data. **B.** Sample GLM components obtained from fits to natural scenes data for an ON parasol cell (same cell in Figure 1.2). **C.** Raster of responses to natural scenes for the same ON parasol cell (black, 55 repetitions). Response structure is only partially reproduced by GLM fitted to natural scenes data. **D.** Comparison of GLM prediction of natural scenes and white noise responses. In each case the GLM was fitted to the same type of stimulus, cross-validated. **E-F.** Same as B-C for a sample OFF parasol cell.

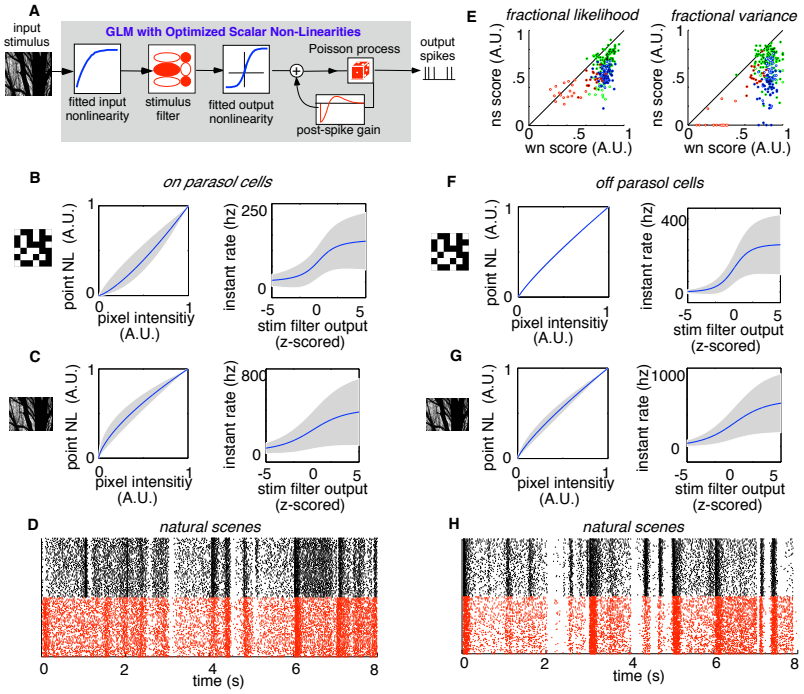

Figure 1.4: **GLM with added scalar nonlinearities performs similarly**. See Figure 1.3 for comparison. **A.** Schematic of the modified GLM, with added nonlinearities highlighted in blue (see text for details). **B.** Nonlinearities for ON parasol cells fitted with white noise data, with 1 SD variability range across cells given by the gray zone. **C.** Same as B, except fitted with natural scenes. **D.** Raster of responses to natural scenes for an ON parasol cell (same cell in Figure 1.2, Figure 1.3). Response structure is only partially reproduced by GLM with additional scalar nonlinearities. **E.** Quantified comparison modified GLM predictions of white noise and natural scenes data. **F-H.** Same as B-D for a sample OFF Parasol Cell.

References

[1] Berry M.J. & Meister M. (1998). Refractoriness and neural precision. *J Neurosci* 18: 2200-2211.

[2] Bialek W., Rieke F., de Ruyter van Steveninck R.R. & Warland D. (1991). Reading a neural code. *Science* 252: 1854-1857.

[3] Chichilnisky E.J. (2001). A simple white noise analysis of neuronal light responses. *Network: Computation in Neural Systems* 12: 199-213.

[4] Chichilnisky E.J. & Kalmar R.S. (2002). Functional asymmetries in ON and OFF ganglion cells of primate retina. *J Neurosci* 22: 2737-2747.

[5] Enroth-Cugell C. & Robson J.G. (1966). The contrast sensitivity of retinal ganglion cells of the cat. *J Physiol* 187: 517-552.

[6] Frechette E.S., Sher A., Grivich M.I., Petrusca D., Litke A.M. & Chichilnisky E.J. (2005). Fidelity of the ensemble code for visual motion in primate retina. *J Neurophysiol* 94: 119-135.

[7] Hochstein S. & Shapley R.M. (1976). Linear and nonlinear spatial subunits in Y cat retinal ganglion cells. *J Physiol* 262: 265-284.

[8] Keat, J., Reinagel, P., Reid, R.C., & Meister, M. (2001). Predicting every spike: a model for the responses of visual neurons. *Neuron, 30*(3), 803-817.

[9] Kuffler S.W. (1953). Discharge patterns and functional organization of mammalian retina. em J Neurophysiol 16: 37-68.

[10] Litke A.M., Bezayiff N., Chichilnisky E.J., Cunningham W., Dabrowski W., Grillo A.A., Grivich M., Grybos P., Hottowy P. & Kachiguine S. (2004). What does the eye tell the brain? Development of a system for the large-scale recording of retinal output activity. *Nuclear Science, IEEE Transactions on* 51: 1434-1440.

[11] Nirenberg S. & Pandarinath C. (2012). Retinal prosthetic strategy with the capacity to restore normal vision. *Proc Natl Acad Sci U S A* 109: 15012-15017.

[12] Olshausen B.A,. Field D.J. (2004). Sparse coding of sensory inputs. *Current Opinion in Neurobiology, 14*: 481-487.

[13] Paninski L. (2004). Maximum likelihood estimation of cascade point-process neural encoding models. *Network Comp. Neural Syst. 15*, 243262.

[14] Pillow J.W., Paninski L., Uzzell V.J., Simoncelli E.P., & Chichilnisky E.J. (2005). Prediction and Decoding of Retinal Ganglion Cell Responses with a Probabilistic Spiking Model. *Journal of Neuroscience* 25:11003-11013.

[15] Pillow J.W., Shlens J., Paninski L., Sher A., Litke A.M., Chichilnisky E.J. & Simoncelli E.P. (2008). Spatio-temporal correlations and visual signalling in a complete neuronal population. *Nature* 454: 995-999.

[16] Pitkow X., Meister M. (2012). Decorrelation and efficient coding by retinal ganglion cells. *Nature Neuroscience* 15: 62835.

[17] Ratliff, C.P., Borghuis, B.G., Kao, Y.H., Sterling, P., & Balasubramanian, V. (2010). Retina is structured to process an excess of darkness in natural scenes. *Proceedings of the National Academy of Sciences, 107*(40), 17368-17373.

[18] Reich D.S., Victor J.D. & Knight B.W. (1998). The power ratio and the interval map: spiking models and extracellular recordings. *J Neurosci* 18: 10090-10104.

[19] Rieke F., Warland D., de Ruyter van Steveninck R.R. & Bialek W. (1997). *Spikes: exploring the neural code.* Cambridge, MA: MIT Press.

[20] Schwartz, G.W., Okawa, H., Dunn, F.A., Morgan, J.L., Kerschensteiner, D., Wong, R.O., & Rieke, F. (2012). The spatial structure of a nonlinear receptive field. *Nature Neuroscience, 15*(11), 1572-1580.

[21] Sharpee T., Rust N.C. & Bialek W. (2004). Analyzing neural responses to natural signals: maximally informative dimensions. *Neural Comput* 16: 223-250.

[22] Shlens J., Field G.D., Gauthier J.L., Grivich M.I., Petrusca D., Sher A., Litke A.M. & Chichilnisky E.J. (2006). The structure of multi-neuron firing patterns in primate retina. *J Neurosci* 26: 8254-8266.

[23] Shlens J., Rieke F. & Chichilnisky E.J. (2008). Synchronized firing in the retina. *Curr Opin Neurobiol* 18: 1-7.

[24] Simoncelli E.P. & Olshausen B.A. (2001). Natural image statistics and neural representation. *Annu Rev Neurosci* 24: 1193-1216.

[25] van Hateren J.H. & van der Schaaf A. (1998). Independent component filters of natural images compared with simple cells in primary visual cortex. *Proc Biol Sci* 265: 359-366.

[26] Williamson R.S., Sahani M., & Pillow J.W. (2015). The Equivalence of Information-Theoretic and Likelihood-Based Methods for Neural Dimensionality Reduction. *PLoS Comput Biol 11*(4): e1004141. doi:10.1371/journal.pcbi.1004141

This chapter presents the main material for the following manuscript:

Heitman, Alexander K.; Brackbill, Nora; Greschner, Martin; Sher, Alexander; Litke, Alan M.; Chichilnisky, E.J. "Testing pseudo-linear models of responses to natural scenes in the primate retina".

The manuscript is in the final stage of preparation and will be submitted soon. The journal is still undecided. Alexander Heitman is the primary researcher of the manuscript and conducted the majority of the analysis, model fitting, and simulation in the paper. Ms. Nora Brackbill provided additional insight and support in various aspects of the project. Dr. Martin Greschner created the original natural scenes stimulus, recorded the original pieces, and was instrumental in formulating the project. Dr. Alexander Sher and Dr. Alan M. Litke developed the multi-electrode array which enables the unique high-fidelity population recordings. Finally Dr. EJ Chichilnisky is the PI of the lab where the research conducted. He was instrumental in formulating the project, provided guidance throughout, and did the majority of the finalized writing for submission. The author is thankful to everyone for their contributions.

Chapter 2

Testing physiologically based modifications of linear cascade models

2.1 Abstract

The previous chapter was dedicated to the inability of the Generalized Linear Model (GLM) and more generally linear filtering, to replicate the retinal ganglion cell (RGC) response to naturalistic stimuli. This chapter analyzes whether including additional physiologically motivated terms would rescue the model and significantly improve the ability to replicate the neural response. The GLM is an ideal model to incorporate these terms due to its innate flexibility and convex fitting. Specifically we analyze whether the inclusion of any of the following would correct the modeling failures: (a) a dynamic cone model, (b) fixational eye-movements, (c) separated excitatory and inhibitory stimulus filters. The general conclusion is that none of these terms were able help replicate the response to naturalistic stimuli. Moreover, disruption of convexity proved to be a serious obstacle when fitting to natural scenes. The results highlight the difficulty of replicating the natural scenes response while also emphasizing the need for models which feature reliable

fitting techniques.

2.2 Dynamic Cone Model – Introduction

The input into the standard GLM is a linear rescaling of the light intensity produced by visual stimulus. The stimulus filter of the GLM is largely meant to describe how the RGCs transforms spatio-temporal light patterns into neural spiking activity. However, preceding the RGC in the neural cascade are neural elements with known non-linear processing. The cone photoreceptors are one known example which features both nonlinearities and dynamic light adaptation. Both of these components are impossible to capture with the initial linear stimulus filter of the GLM.

To account for this we incorporate a non-linear dynamical systems model of the cone photoreceptors (see Figure 2.1A for schematic, J.M. Angueyra and F. Rieke personal communications). The model is biophysically derived, and is meant to capture the full non-linear dynamics of the cone photoreceptor response to light stimulation. The output of the model is subsequently used as a modified input into the GLM (Figure 2.2A). Testing the newly fitted GLM thus theoretically answers whether accounting for the cone dynamics enables a more accurate response reproduction for naturalistic stimuli.

2.3 Dynamic Cone Model – Methods

The dynamic cone model was developed by collaborators from the University of Washington and consists of a six equation system of non-linear differential equations (see Figure 2.1A for schematic, J.M. Angueyra and F. Rieke, personal communications). The model is derived from patch recordings of primate cones and attempts to capture the full biophysical cascade, starting with photo-isomerization and ending with current input into the cone outer segment. The full details of the model have yet to be published and the model is used by this author in an black box manner.

The lone parameter necessary to run the model is an approximate count of cone photo-isomerizations generated by the light stimulation each second. The parameter was

roughly 5000 isomerization per second for the average stimulus intensity for the long and middle wavelength cones, and a more full description is in the methods section of chapter one. As an additional control, the model was run with this parameter tested at .1x, 10x, 100x of the measured value to demonstrate robustness of the results. All results remained the same despite rescaling.

Each independent block of pixels were run separately through the cone model. Thus the model provided point by point transformation and treated the cone layer as an effectively continuous layer. The output of the model was then used as a modified input into the GLM (Figure 2.2A). The rest of the GLM was identical to what was used in chapter one and is described in the methods of chapter one.

2.4 Dynamic Cone Model – Results

First, the authors verified that the output of the cone model added non-linear variation to the input. The nature of the changes to the light signal shows a mixture of temporal decay and non-linear stretching (Figure 2.1B). Those changes would be impossible to generate with the linear filter of the GLM. Second, the authors verified that the fitted stimulus filter of the GLM reflected the changes to the model input. It is clear that the temporal component in particular exhibits a fundamental change, appearing closer to a fast derivative operator than before (Figure 2.2B). In summary, the dynamic cone model provides dynamic non-linearities to the stimulus input and this change is reflected by the altered time course of the stimulus filter.

However, despite the changes, the cross-validated test repeats generated from the GLM show no improvement and fail in nearly an identical manner as the original model (Figure 2.2E). When quantified with fractional likelihood (measure developed in Chapter 1 Methods 1.4), the cross-validated white noise and natural scenes performance shows no change (Figure 2.2C). Moreover, it follows that the observation that natural scenes performance is inferior to white noise performance remains robust (Figure 2.2D). Though not pictured, the results are the same when using the fractional variance metric as well.

2.5 Dynamic Cone Model – Discussion

The lack of improvement induced by the dynamic cone model suggests that dynamic non-linearities in the photo-isomerization to current transformation in the cones is not the source of failure of the GLM with natural scenes. Moreover, the fact that the performance is indistinguishable from the standard GLM (Figure 2.2C, 2.2E) suggests that despite the non-linearities, the transformations are largely invertible by the linear filter. This could represent a deficiency in applying the cone model to our preparation; however, it is also likely that the source of failure lies somewhere else in the retina. Regardless, checking the dynamic non-linearities at the origin of the visual signal is an important first step and provides a good start for ruling out failure sites.

2.6 Fixational Eye Movements – Introduction

A feature of the naturalistic stimuli, and moreover natural vision, which is utterly absent from the white noise stimuli is the presence of fixational eye movements (FEM) (Martinez-Conde2004[3]). An explanation of the FEM used can be found in methods section of chapter one. Though the interaction of the GLM stimulus filter with the visual stimulus does pick up changes in the light patterns due to local changes induced by FEM, the GLM still lacks a mechanism to track the potential modulations of the visual response due to the larger phenomena of FEM. Though a physiological justification can not be directly identified, the authors seek a computational mechanism to test for the effect of FEM.

Given the flexible structure of the GLM, this can be easily accommodated by including the FEM traces as a new covariate of the model and subsequently adding an FEM filter to the GLM (schematic in Figure 2.3A). Testing the GLM with FEM thus provides a clue to whether FEM is indeed a source of error and whether accounting for FEM significantly improves the ability of the GLM to replicate the response to natural scenes.

2.7 Fixational Eye Movements – Methods

The original fixational eye movements consisted of horizontal and vertical traces of displacements binned at the monitor refresh time of roughly 8.3 milliseconds ($120\,hz$). These were combined into a single positive scalar trace by computing squared displacements of the eye movements at the 8.3 millisecond bin rate. This squared displacement (single trace) was provided as a new input into the GLM (Figure 2.3A).

The GLM was then modified with a linear FEM filter which essentially described an impulse response with respect to FEM displacement. The convolution was then added to the output of the stimulus filter before being run through the exponential non-linearity (Figure 2.3A). The impulse response tested rate fluctuations for a 583 millisecond window (166 milliseconds before and 417 milliseconds after the displacement). The impulse response was also binned at 8.3 milliseconds and thus added a total of sixty parameters to the GLM. The remainder of the GLM was unchanged.

2.8 Fixational Eye Movements – Results

First, the authors verified that the fitted FEM filters were viable. The fitted filter were smooth in nature and showed no significant signal for time preceding the FEM, passing causality of impulse responses (Figure 2.3B). Fitted FEM filters showed a sustained positive response, starting near $0\,ms$ after the FEM and ending before $166\,ms$ (Figure 2.3B). This sort of filter was uniform to nearly all cells. While preparation and celltype heterogeneities existed, the sustained positive response was consistent (Figure 2.4).

However, despite the consistent ability to fit a viable FEM filter, the cross-validated test repeats generated from the GLM with FEM showed no improvement and fail in nearly an identical manner as the original model (Figure 2.3E). When quantified with both fractional likelihood and fractional variance (measure developed in Chapter 1 Methods 1.4), the cross-validated natural scenes performance shows only modest improvement (Figure 2.3C). Moreover, it follows that despite the additional 60 parameters used for only natural scenes, the observation that natural scenes performance is inferior to white noise performance

remains robust across both metrics (Figure 2.3D).

2.9 Fixational Eye Movements – Discussion

The consistent fitting of the FEM filters (Figure 2.4) suggests that there indeed exists a modest signal induced by FEM. However, the signal is uniformly small and the lack of improvement in the simulated repeats suggests that the source of failure of the GLM with natural scenes is not related to FEM. The fact that the natural scenes inferiority remains despite an additional 60 parameters makes the failure even more striking. This could either represent a deficiency in how the GLM incorporated FEM; perhaps creating a linear impulse response to displacement at the binned time scale was not optimal. However, the presence of a clear reproducible signal suggests otherwise. The authors thus hypothesize that neither dynamic cone non-linearities nor fixational eye movements are the primary source of the failure to reproduce the response to naturalistic stimuli.

2.10 Conductance Based Model – Introduction

Like most models based in linear filtering of the stimulus, the GLM filter is responsible for both driving and inhibiting the model cell. However, it is thought that the source of excitatory and inhibitory synaptic input to the retina ganglion cell (RGC) is likely to have different neural sources (Cafaro2013[1]). To roughly account for this and probe for additional spatio-temporal signals we combine a recently developed "onductance-based" model (Latimer2014[2]) with the GLM. Rather than having a single stimulus filter the conductance based GLM (CBGLM) features an excitatory stimulus filter as well as an inhibitory stimulus filter.

Unfortunately the CBGLM breaks convexity and therefore does not guarantee convergence. However, the potential of two separate filters which could uncover different neural components was tried for both natural scenes and white noise.

2.11 Conductance Base Model – Methods

The GLM was modified into the CBGLM by doubling the stimulus filter count. Both filters received the same visual input, but they were then fed into opposite rectifying nonlinearities (Figure 2.5A). The first "positive rectifier" only kept the output of the filter which resulted in positive gain. This was done with a strict rectifier which was the identity for positive values and zero for negative values. This made the corresponding filter effectively an excitatory filter. An opposite rectifier which only passed negative signals shaped the inhibitory filter. The output of the two filters were summed and run through the standard exponential nonlinearity to generate the stimulus driven rate. The remainder of the model is identical to the original GLM. This nearly doubled the parameter count, raising it from 220 to 419.

2.12 Conductance Base Model – Results

The first main result is that the lack of convexity resulted in poor fits for the natural scenes (Figure 2.5B). The author is not sure what techniques could be employed to rescue convergence. However, the author is confidant that an unassisted automated maximization of objective value will not be sufficient to properly fit the model to natural scenes.

The lack of convergence, however, does not indicate that the CBGLM is inherently inadequate. However, there are hints in the white noise fits which indicate that even a properly fit CBGLM will not reproduce the response to natural scenes. For the same cell which exhibited poor fitting in NSEM, clear filters are fitted with white noise (Figure 2.5C). However, these filters do not indicate any heterogeneity, neither in space nor in time. It seems that the two filters are merely replicating a single filter split in two by the respective rectifying nonlinearities. This is reflected in the scores associated with the white noise fits (Figure 2.5D). Despite nearly doubling the parameter count, the CBGLM is only marginally better than the GLM, if not at all. When comparing with a GLM with two filters but no rectification, the CBGLM is slightly worse. There are no indications that splitting into two

filters by rectifying nonlinearities cause any significant improvement with white noise.

Thus the CBGLM does not consistently fit the natural scenes. However, since the CBGLM doesn't help with white noise, it is likely that even a properly fitted CBGLM would not be able to reproduce the natural scenes response.

2.13 Conductance Base Model – Discussion

The meager improvement in white noise fits by the CBGLM, despite doubling parameter count, is certainly disappointing. Asides from casting doubt on the ability of the CBGLM to reproduce the natural scenes response, the breakdown of consistent convergence with natural scenes is noteworthy. The rectifying non-linearities represent a break from convexity, but that break should be relatively minor. These results strongly indicate that for automated model fitting with natural scenes, use of a convex model is likely to be a necessity.

2.14 Figures

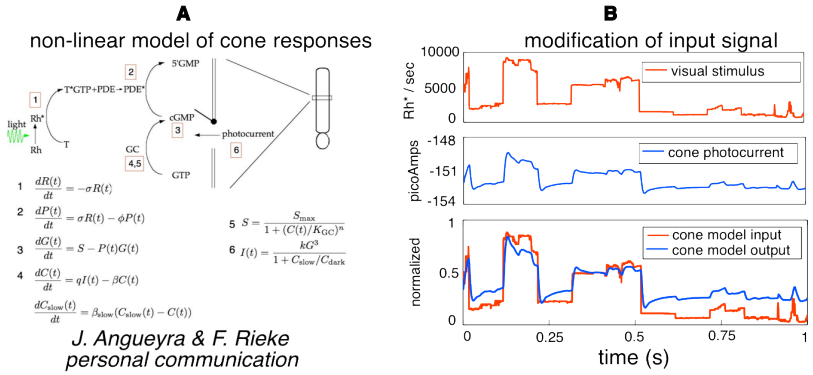

Figure 2.1: **Dynamic Cone Model**. **A.** Cartoon schematic of the biophysical cascade being modeled followed by the corresponding differential equations. Models the cascade from photo-isomerization to photocurrent flux into the cone. **B.** Sample traces of how the model input in photoisomerizations per second (red traces) gets transformed to the model output of cone photocurrent (blue traces). The overlay indicates that in addition to some temporal smoothing, there exists non-linear rescaling.

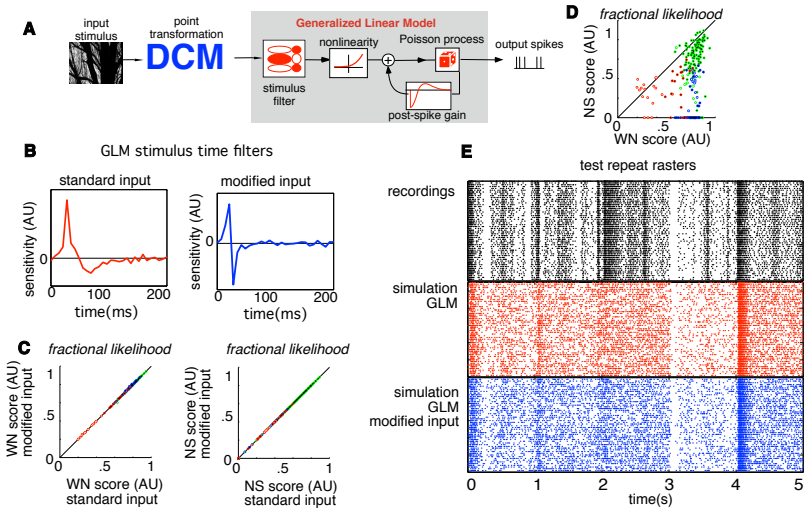

Figure 2.2: **Incorporating Dynamic Cone Model into the GLM**. **A.** Schematic of how the dynamic cone model (DCM) was incorporated to modify the GLM input. The DCM operated on each independent block of pixels resulting in essentially a point transformation meant to mimic a similar transformation by the entire cone photoreceptor layer. The rest of the GLM is unaltered. **B.** Modifying the GLM input by incorporating the DCM resulted in qualitatively different temporal properties of the stimulus filter. The long inhibitory phase of the original filter (red trace) is replaced with a much sharper switch like operation (blue trace). This change was consistent across all cells. **C.** Modifying the input by the DCM did not produce any change in cross-validated scores for both white noise and natural scenes. Fractional variance (not shown) also has the same result. **D.** Modifying the input by the DCM still leads to the same comparison between white noise and natural scenes. Natural scenes reproduction is still clearly inferior (same holds with fractional variance, not shown). **E.** Single cell example showing that the reproduced rasters with the DCM (blue) show the exact same failures as with the original GLM (red) in trying to reproduce the recorded test repeats (black).

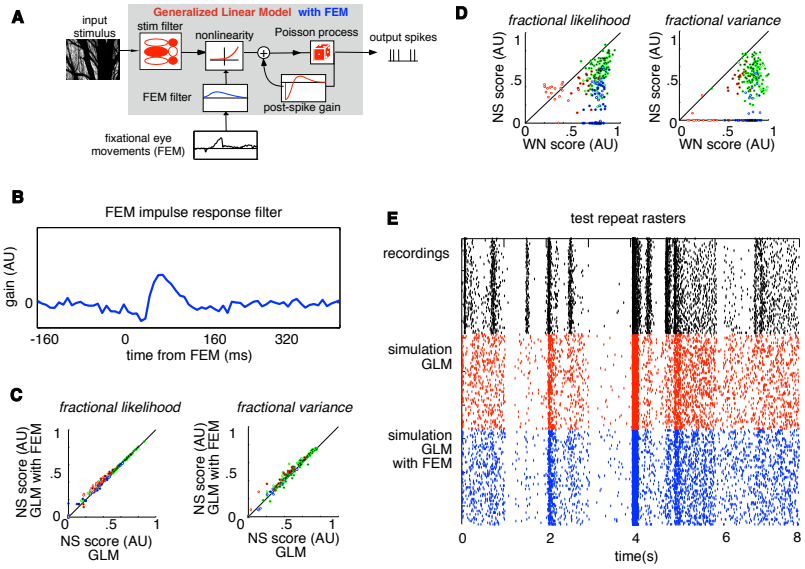

Figure 2.3: **Incorporating Fixational Eye Movements into the GLM**. **A.** Schematic of how fixational eye movements (FEM) were incorporated to modify the GLM. FEM traces were transformed to scalar displacement traces seen in black (see Methods 2.7). An FEM filter (blue) then linearly convolved the displacement traces to modulate the model's firing rate. FEM filter effectively represents a linear impulse response to the displacement cause by FEM. The rest of the GLM remained unchanged. **B.** Sample fit of the FEM filter. The filter is smooth, passes causality (no signal at times before zero), and uniform across nearly all neurons. Less than 20% of fits featured only noise, signals all took this form. **C.** Modifying GLM with FEM for natural scenes produced only a modest improvement in fractional likelihood and had minor mixed results for fractional variance. **D.** Modifying the GLM with FEM still leads to the same comparison between white noise and natural scenes. Natural scenes reproduction is still clearly inferior despite the additional parameters used only for natural scenes in the FEM filter. **E.** Single cell example showing that the reproduced rasters with FEM (blue) show the exact same failures as with the original GLM (red) in trying to reproduce the recorded test repeats (black).

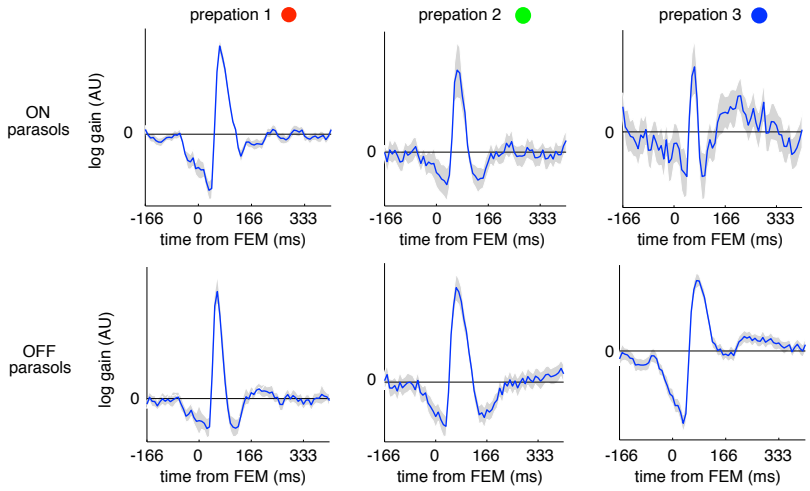

Figure 2.4: **Distribution of fixational eyemovement (FEM) filter fits**. All fitted FEM filters split up by preparation (columns, color dots match in Figure 2.2CD Figure 2.3CD), and celltype (rows). Blue traces represent the average population signal. Gray background represents plus or minus 3 times the SEM. All exhibit positive gain signal within the interval of 0 to 166 ms. Behavior before and after these time points show some heterogeneity.

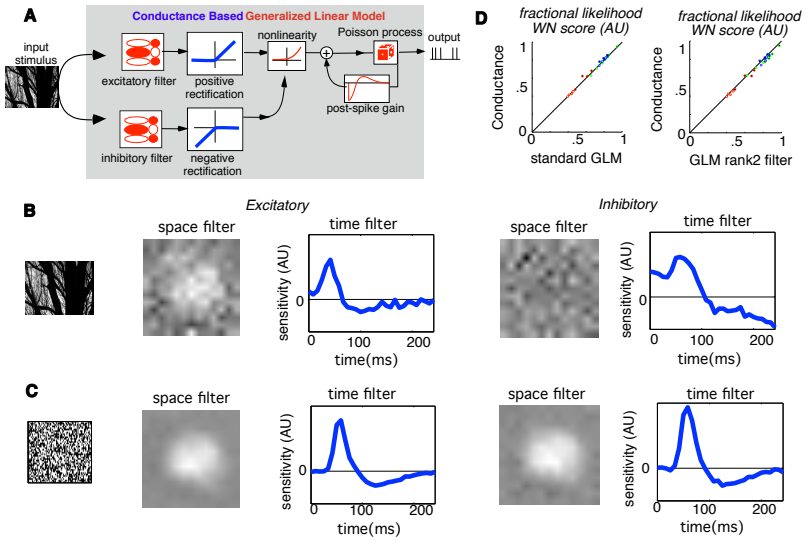

Figure 2.5: **Conductance Based Model Fits**. **A.** Schematic of the conductance based model. Two stimulus filters are used and run through an additional rectifying non-linearity. Rectifiers permit only positive gain (excitatory filter) or negative gain (inhibitory filter). The remained of the model is identical to the GLM. Note that the inclusion of rectifying nonlinearities disrupts convexity. **B.** Sample natural scenes fit which failed to properly converge. The excitatory filter shows hints of receptive field structure in the spatial filter and time filter. Inhibitory filter fits nothing, probably due to failed convergence. **C.** Sample white noise fit from the same cell. White noise showed clear signal convergence. The excitatory and inhibitory filters are largely the same. **D.** Conductance based model despite nearly doubling the parameter count only marginally improves white noise scores (left panel). When compared to an equivalent parameter count rank-2 linear spatial filter, it does slightly worse (right panel).

References

[1] Cafaro J., & Rieke F. (2013). Regulation of spatial selectivity by crossover inhibition. *The Journal of Neuroscience, 33*(15), 6310-6320.

[2] Latimer K.W., Chichilnisky E.J., Rieke F., & Pillow J.W. (2014). Inferring synaptic conductances from spike trains with a biophysically inspired point process model. *In Advances in Neural Information Processing Systems* (pp. 954-962).

[3] Martinez-Conde S., Macknik S.L., & Hubel D.H. (2004). The role of fixational eye movements in visual perception. *Nature Reviews Neuroscience, 5*(3), 229-240.

Chapter 3

Analyzing stimulus polarity and edge configurations to examine neural factors underlying the Westheimer effect in peripheral vision

3.1 Abstract

The Westheimer curve is a well-documented visual phenomena which analyzes how the detection of a test-pulse of light over a gray background depends on the size of the background (Westheimer2004 [12]). The observed curve firmly establishes the non-local nature of visual detection. Moreover, the bi-phasic nature of the curve encourages parallels with the center-surround organization of visual neurons in the retina. Two dominant narratives have emerged to explain the Westheimer curve. The first narrative combines classic center-surround antagonism of visual neurons with saturating neural responses to excitatory drive to explain the curve. The second narrative hypothesizes that the curve is

largely due to the presence of an edge.

The Westheimer curve is typically constructed from test-pulses which are brighter than the gray background and surrounding regions which are darker than the gray background. This study systematically examines alternative stimulus polarity configurations as well as edge configurations to determine the validity of the two dominant narratives.

3.2 Introduction

The Westheimer curve is a well-documented visual phenomena in which the threshold for detection of a small test-pulse of light is raised when the surrounding visual area is darkened (Figure 3.1A, B, see Westheimer2004 [12] for review). This classic result firmly establishes the importance of non-local lateral interactions in perhaps the most basic of visual tasks, detecting a pulse of light (Crawford1940 [1], Westheimer1965 [10], Westheimer1967 [11]). Moreover, the biphasic nature of the Westheimer curve bears a striking resemblance to the dual nature of center-surround antagonism of visual neurons, particularly in the retina. This phenomenological overlap makes the effect an enticing target for linking perception to neural factors. However, despite the long deep literature concerning the Westheimer Effect the exact neural locus and mechanism is still unclear (MacLeod1978 [7], Westheimer2004 [12]). Neural center-surround antagonism is a common feature of visual neurons at all levels in early processing (photoreceptors, bipolar cells, retina ganglion cells LGN, and early visual cortex) and is not sufficient to locate the neural factors governing the Westheimer effect. Some evidence exists which suggest a cortical locus, while other evidence suggests retinal locus; the discrepancies are a reflection of the challenge of establishing neural loci with pure visual psychophysics.

Despite the discrepancies, the dominant narrative which drives interest in the phenomena is a linking hypothesis which combines classic center-surround antagonism of visual neurons with saturating neural responses to excitatory drive (further explained in Experiment 1). A second narrative is that the effect is driven primarily by the presence of a hard edge (Lennie1973 [6]). Edge effects are generally suggestive of a downstream cortical

locus or a retinal locus based upon fixational eye-movements. In order to parse apart the potential factors, this study will systematically analyze stimulus polarity configurations and edge configurations. The logic of the entire study heavily relies on the presumption that the threshold of increment detection is mediated by the ON pathway and that the threshold of decrement detection is mediated by the OFF pathway. While no experiment has directly demonstrated this in human vision, there exists strong evidence from Macaques directly linking pharmacological manipulation at the earliest stage of ON and OFF pathway segregation (bi-polar layer) to behavioral detection of light increments and light decrements (Schiller1986 [9]). The rest of this article will be written under the presumption that this finding generalizes to human vision.

This study consists of four experiments and one additional analysis section. The aim of Experiment 1 is to test the qualitative robustness of the center-surround linking hypothesis by switching the polarities of both test-pulse and the surround. The aim of Experiments 2 and 3 are to account for the role of both edge effects and fixational eye movements. Experiment 4 returns to the center-surround linking hypothesis to cast additional doubt on its validity, in favor for a mundane interpretation based upon limited stimulus resolution. The additional analysis summarizes the asymmetries in increment vs. decrement detection that are present in the data collected from Experiments 1–4.

The issues raised in Experiments 1–3 have been similarly analyzed under slightly different conditions in the following studies (Sinai1999 [8], Lennie1973 [6], Kunken2005 [5]) (more in Discussion 3.4). Most notable is a foveal study (Sinai1999 [8]) which both demonstrated an OFF pathway analogue to the Westheimer curve and hypothesized that the summation of both the center-surround linking hypothesis and edge effects explains the Westheimer curves. Despite some overlap in development, this peripheral study generates a considerable amount of data and conclusions which differ from the previous studies. This study suggests that combining the center-surround linking hypothesis with edge effects remains insufficient to explain the Westheimer curves. Moreover, this study infers that the bi-phasic nature of the Westheimer curve is likely unrelated to center-surround receptive fields.

3.3 Methods

Subjects

The study is centered about three heavily trained subjects (S1,S2,S3), who participated in all four experiments. S1 is the author, S2 is a devoted volunteer, S3 is an undergraduate lab member. Experiments 2–4 each feature an additional untrained volunteer (S4,S5,S6). Only the author S1 was fully aware of the research questions being addressed. All subjects were willing participants and the procedures followed the IRB guidelines delineated in UCSD 081130.

Stimulus Delivery

An HP Dream Color was placed 1.2 meters in front of the subjects. Precision was increased from 10 bits to 13 bits by incorporating Cambridge Research Systems Bits++ hardware device. The monitor was carefully gamma calibrated and proved to be a suitable replacement to the traditional CRT monitor.

Detection Tasks

Subjects performed detection tasks for test-pulses of achromatic light that were brighter than the gray background (incremental test-pulses) and test-pulses which were darker than the gray background (decremental test-pulses). Thresholds were found for a variety of background sizes, with either an achromatic dark surround ($\sim$ 0 candelas per meter squared) or an achromatic light surround ($\sim$ 200 candelas per meter squared). The gray background was always held at $\sim$ 50 candelas per meter squared.

Detection for all experiments was determined using a spatial four alternative forced-choice paradigm (Figure 3.3A). Four square steady gray backgrounds were symmetrically placed in each quadrant centered $\sim$ 8 degrees in the periphery. The square test-pulse had a width of $\sim$ 13 minutes of arc and randomly occurred in the center of one of the four backgrounds. Test-pulses were 200 millisecond ramps (Figure 3.3B) with a fast onset, followed by a slow 200 millisecond linear decay back to gray. Ramps were chosen over steps to ensure that threshold detection was attributable to test-pulse onset, hence incremental test-pulses were detected on the incremental onset rather than the decremental offset.

Assuming that results of (Schiller86 [9]) are generalizable to human psychophysics, the incremental test pulses are thus detected by the ON pathway and decremental test pulses are detected by the OFF pathway. The size of the background was systematically varied from the size of the test-pulse and ranged from ~ 13 minutes of arc up to to the full span of the monitor (referred to as the uniform background condition).

Data Collection Procedures

Due to the demanding nature of threshold detection in the periphery, all data were gathered in short sessions of thirty minutes to ensure alert observations. Each session measured a single pair of incremental and decremental thresholds for a single background size and a single surround polarity. Incremental and decremental trials were randomly interspersed in the same session and while performing near threshold, subjects were unable to distinguish between the trials. During all trials subjects were instructed to maintain fixation on a central fixation target. The combination of a forced-choice paradigm, the inability to distinguish increments from decrements at threshold, and random interweaving of increment and decrement test-pulses all combine to make a task which stably measures the differences in threshold for incremental and decremental test-pulses.

For quality control, all observers were adapted to indoor light levels for at least a half hour before each session. Moreover each session began with warm up practice trials to acclimate the subject to the detection task. Each session consisted of 200–400 trials, with longer sessions resulting in fatigue and unreliable data. Finally, subjects had the option to take a one minute recovery period every 50 trails within each data collection session.

Defining Threshold

Intensity values of the test-pulse were modulated with a staircase procedure programmed to hone in on 62.5% accuracy. The staircase generated psychometric curves which were subsequently fit by cumulative gaussians (μ, σ) with a likelihood maximization procedure. The estimate of the μ parameter of the fitted cumulative gaussian was deemed to be the threshold.

Defining P Values of threshold comparisons

When comparing the threshold for two sets of detection trials from two different

conditions (A,B), the P-values can be computed under the following formulation. (CG = Cumulative Gaussian)

$$\text{Prob (detect | condition = A, stimulus = x)} \sim CG(\mu_A, \sigma_A, x)$$
$$\text{Prob (detect | condition = B, stimulus = x)} \sim CG(\mu_A + \mu_{B-A}, \sigma_B, x)$$
$$H0 : \mu_{B-A} == 0$$
$$HA : \mu_{B-A} \sim= 0$$

Under this formulation define MLE_0 to be the most likely estimator of the parameters under the null hypothesis and MLE_A to be the most likely estimator of the parameters under the alternative hypothesis. Following Wilkes Theorem (Wilks1938 [13]) it follows that negative two times the logarithm of the likelihood ratio asymptotically follows a *chi*-squared distribution with one degree of freedom. The high number of observations (200–400) and low number of parameters (four) should justify the asymptotic approximation.

$$-2 * \log(likelihood(data|MLE_0)/likelihood(data|MLE_A)) \sim Chi - Squared(DOF = 1) \tag{3.1}$$

Alternatively, Bayes Factors have also been approximated from the most likely estimators using both the Akaike Information Criterion as well as the Bayes Information Criterion (Kass1995 [3]). The resulting interpretation of significance is the same as what is seen with P-values from the likelihood ratio, suggesting robustness of the statistical analysis.

Blurred edge in Experiment 2

The background width was fixed at $\sim$ 36 minutes of arc, near where the traditional Westheimer Effect is maximized. Rather than a sharp transition to the surround (.7 minutes of arc for Experiment 1), the surround was not fully dark or light until after transitory linear gradient of 18 minutes of arc on each side (schematic in Figure 3.5A). Subjectively all three experienced subjects clearly noticed the blurring. The rest of Experiment 2 was methodologically identical to Experiment 1.

Double edge Normalizer in Experiment 3

As a means of establishing a lower bound on the effect of a high-contrast edge, increment and decrement detection was performed over a gray uniform background with two square rings (inside white, outside black) resulting in three successive high-contrast edges (schematic Figure 3.6A). The inside ring has an inner width of 36 minutes of arc and outer width of 45 minutes of arc and intensity of $\sim$ 200 candelas. The adjacent outside ring has an inner width of 45 minutes of arc and outer width of 54 minutes of arc and intensity of $\sim$ 0 candelas. The intensity on the inside and outside of the double rings was the same gray of $\sim$ 50 candelas. This was repeated a second time with a black inner ring and white outer ring.

Zero flux test-pulse in Experiment 4

A test-pulse which resulted in $\sim$ 0 change in photon intensity was constructed. The "zero-flux test-pulse" was square with same dimensions as the incremental test-pulses (width $\sim$ 18 minutes of arc) and consisted of four equally sized horizontal bars of light (schematic on Figure 3.7A). From top to bottom each bar was either (decremental, incremental, decremental, incremental) or (incremental, decremental, incremental, decremental) to the gray background. The magnitude of the increments and decrements were varied on the staircase, but their added sum always led an average intensity equal to that of the gray background. This minimized the amount of stray light which penetrated the surround and was meant to provide a more precise measurement of how a dark surround modulates the sensitivity of the cells in the background (the theoretical goal of the Westheimer curves).

Experiment 1: Introduction

Experiment 1 will have the strict focus of testing the center-surround linking hypothesis by probing its ability to generalize to different polarities of both the test-pulse and the surround. The traditional Westheimer Effect describes the threshold of detection of incremental test-pulses of light over a gray background with a dark surrounding region (Figure 3.1). Experiment 1 generalizes the effect by analyzing four variants: dark surround with incremental test pulse (classic Westheimer), dark surround with decremental test pulse, light surround with incremental test pulse, light surround with decremental test

pulse (see Figure 3.2A).

The logic of the experiment is based upon an extrapolation of the classic linking hypothesis of the Westheimer curve. In short, the hypothesis claims that increments are detected by an on-center off-surround visual neuron with a saturating response to excitatory drive (1C 1D). Compared to a uniform gray background, the cell is relatively more excited by a tonic dark stimulus placed in the cell's off-surround. This increased excitation leads to a more shallow portion of the cells response curve (1D), resulting in less sensitivity to the test-pulse and hence a raised threshold (1E). As the gray background shrinks, the dark stimulus excites a larger portion of the cell's off-surround and the threshold continues to get raised. This presumably is reflected in Figure 3.1B, where shrinking the background width from 100 minutes of arc to 50 minutes of arc results in further increased thresholds. However, once the background is too small, then the dark surrounding stimulus begins to inhibit the on-center of the cell and initiates the bi-phasic nature of the curve. The inhibited on-center lowers the excitation, raising the sensitivity and hence lowering the threshold. Presumably this is reflected in Figure 3.1B by the decline in threshold as the background shrinks from 36 to 18 minutes of arc.

Figure 3.2B and 3.2C demonstrates an extrapolation of the exact same logic to the four stimulus polarity configurations in 3.2A. Explicitly, one would expect that decrement detection over a light surround (fourth column) to be qualitatively identical to the Westheimer curve and thus yield an Off-Pathway analogue of the curve (Sinai1999 [8]). Moreover, both increment detection with a light surround and decrement detection with a dark surround would qualitatively yield an "inverted" Westheimer curve. For the remainder of the article the figures will follow the color convention, red highlighting indicates light surrounds, blue highlighting indicates dark surrounds, white dots indicate increment detection, black dots indicate decrement detection.

Experiment 1: Results

The results gathered convey two clear observations which are uniform across all three subjects and directly contradictory to the linking hypothesis. (Figure 3.4A compare to Figure 3.2).

First is the complete lack of an "inverted" Westheimer curve for increment detection over a light surround and decrement detection over a dark surround. In both of these cases, the surround theoretically should lower tonic excitation levels, making the detecting cell more sensitive hence lowering the threshold. However, results over every background width indicates the exact opposite; the presence of contrast in the surrounding stimulus, whether light or dark, always raises the threshold (Figure 3.4A). The classic Westheimer curve peaks at roughly 36 minutes of arc. At this background width, all four stimulus configurations are unequivocally above the uniform threshold contradicting expectations of the linking hypothesis (Figure 3.4B). This strongly suggests that an inhibitory surround coupled with saturating neural response is (Figure 3.1C, D) is an insufficient explanation of the Westheimer curve. Similar conclusions have been drawn with similar results in previous studies (Sinai1999 [8], Kunken2005 [5], Lennie1973 [6]).

The second contradiction of the linking hypothesis is the lack of biphasic behavior in the light surround conditions. When the surround is brighter than the background, both increment and decrement detection increase monotonically as the width of the background shrinks (Red Curves Figure 3.4A). This is quantified by comparing the thresholds at the smallest background width and at the background width which maximizes the classic Westheimer curve, 18 and 36 minutes of arc respectively. With the dark surround, the thresholds for both increment and decrement detection are lower with a background width of 18 than with a background width of 36; however, with the light surround the opposite is true (Figure 3.4C). The monotonicity observed with the light surrounds are in sharp contrast to the bi-phasic OFF pathway Westheimer curve seen in the foveal study (Sinai1999 [8]).

The observed monotonicity calls into question the linking hypothesis which suggests that the bi-phasic nature of the original Westheimer curve (blue curve with white dots Figure 3.4A) is attributable to the transition from the neuron's OFF surround to ON center. An alternative hypothesis is that the detection of light pulses with a small background is mediated by cells whose receptive field lie in the surrounding region but receive spillover light due to the imperfect optics of the human eye. Experiment 4 follows up on this

alternative hypothesis.

Experiment 2: Introduction

Edge effects are numerous in vision, and the general lack of inverted Westheimer curves in Experiment 1 could indicate that edges may be the dominant factor raising the thresholds. In particular it is notable that in Figure 3.4B that with the dark surround increment detection threshold is raised more than decrement detection threshold. One could hypothesize that contrast in the surround provides a hard edge in the visual field which uniformly raises the threshold under surround polarity configurations, and that this is the main force underlying the Westheimer curves. In Experiment 2 we test this hypothesis by first fixing the background width at 36 minutes of arc (width which maximizes classic Westheimer curve) and then blurring the edge from a sharp edge to a linear gradient which spans ~ 18 minutes of arc (Figure 3.5A, see Methods 3.3). Subjects then performed the same detection task over all four stimulus polarities, this time with the edge effect theoretically removed.

Experiment 2: Results

All subjects clearly perceived the blurring of the edge. The qualitative results of the detection thresholds are largely the same as what is seen in Experiment 1 (compare Figure 3.4B with Figure 3.5B). Even with the hard edge removed, the thresholds in all situations are raised, again contradicting the linking hypothesis (Figure 3.5B). These results indicate that the presence of a high contrast edge is not the main factor underlying the uniform raise in threshold from Experiment 1. Thus the contradiction of the central linking hypothesis from Experiment 1 is robust to perceptual blurring of the edge.

Experiment 3: Introduction

In Experiment 2 the edge effect was tested by removing the perceptual hard edge by blurring the transition from the stimulus background to the surround. In this experiment, the effect of the edge is controlled by testing a more specific interpretation of how the edge could raise thresholds. One specific hypothesis concerning the Westheimer curve is that fixational eye-movements are the primary cause of the increase in threshold. The theory hypothesizes that in the absence of the fixational eye-movements, the visual neurons whose

receptive fields lie within the gray background never interact with the surround or the high contrast edge between the background and surround. However, involuntary fixational eye-movements constantly force the high contrast edge to enter into the cell's receptive field, tonically exciting these cells. Because the detecting cells are tonically excited, their sensitivity is lowered which in turn raises the threshold for test-pulse detection.

Experiment 3 seeks to control this effect by introducing a new normalizing threshold. In Experiments 1 and 2 all thresholds were normalized by the detection threshold over a uniform gray background. In Experiment 3, the standard normalizer is augmented by the detection threshold of a test-pulse with a uniform gray background augmented with a high-contrast double square ring of white and black (Figure 3.6A, see Methods 3.3). This is meant to introduce a functional overestimate of the combination of edges and fixational eye-movements without any surround effects. Theoretically, a fixational eye-movement would now drive the visual neurons over three high-contrast edges, exciting the cell at an even higher rate than what could be attributed to the edge in the standard Westheimer curves from experiment one. It follows that normalizing by this threshold will then properly account for the fixational eye-movement hypothesis. One would then expect that either the entire effect is accounted for by the edges, or that controlling for the effect would rescue the validity of the original center-surround linking hypothesis.

Experiment 3: Results

All subjects clearly perceived the presence of the two square rings. The qualitative results of detection thresholds are again largely the same as what is seen in Experiment 1 (compare Figure 3.4B with Figure 3.6B). Even with the edge effect removed, the thresholds in all situations are raised, again contradicting the linking hypothesis (Figure 3.6B). The same holds true when the polarity of the rings are reversed (Figure 3.6C). These results indicate that the interaction of fixational eye-movements across high contrast edges is not the main factor underlying the uniform raise in threshold from Experiment 1 (Figures 3.4A and 3.4B). Moreover the contradiction of the center-surround linking hypothesis is robust to multiple accounts of edge effects.

Experiment 4: Introduction

In Experiment 1 it was observed that for the light surrounds, the observed Westheimer curves were not bi-phasic but rather monotonic (red curves Figure 3.4A and 3.4C). This calls into question the interpretation that the bi-phasic nature of the original Westheimer curve is in-fact due to the center-surround transition of the detecting visual neurons. One alternative hypothesis is that when the surround is dark and the width of the background is small, the test-pulse detection is mediated by cell's in the surrounding region. These cell's in theory could be detecting spill-over light from the test-pulse due to the imperfect optics of the eye. This interpretation is made more plausible given that both the author (subject 1) and a naive observer (subject 2) reported that detection over the smaller backgrounds with the dark surround were subjectively different from all other detection tasks.

To test this peripheral detection hypothesis, a new test-pulse was constructed which had no net flux of light and would therefore generate very little stray light. The test-pulse is a horizontal grating consisting of four horizontally oriented bars, alternating between increments and decrements (schematic in Figure 3.7A, see Methods 3.3). In theory this test-pulse wouldn't generate much stay light and thus it's detection would need to be mediated exclusively by cells whose receptive fields lie within the gray background and not by cell's in the surround. It follows that with a dark surround, the behavior of the detection curve under small background conditions should represent a more accurate depiction of how the dark surround affects test-pulse detection in the absence of the possibility of peripheral detection of stray light.

Experiment 4: Results

In stark contrast to the classic Westheimer curve, the observed Westheimer curves with a dark surround and zero flux test-pulse is clearly not bi-phasic, as the threshold rises monotonically as the background size decreases (compare Figure 3.4A with Figure 3.7B). The comparison of thresholds with background widths of 18 and 36 minutes of arc indicate that with the zero-flux test-pulse, the threshold for the smallest background is indeed the highest. Thus with the zero-flux test-pulse the effect of the dark surround is qualitatively identical to how the light surround modulates incremental and decremental test-pulse de-

tection in experiment 1 (compare Figure 3.4C and Figure 3.7C).

This result provides a line of evidence that with a dark surround, shrinking the background monotonically raises the threshold of detection of the cell's lying at the center of the background. This strongly suggests that the bi-phasic nature of the original Westheimer curve (dark surround, increment detection), is not due to a hypothetical transition from a receptive field's ON center to OFF surround. Rather, the authors hypothesize that the correct interpretation, given known optical imperfections of the eye, is peripheral detection of stray light by visual neurons in the dark surround.

Additional Analysis of Asymmetry

The original linking hypothesis predicts stark asymmetries in increment vs decrement detection as a function of the surround. Experiments 1–3 demonstrate insufficiencies of this linking hypothesis by showing qualitative similarities, namely a uniform raise of threshold (Figures 3.4A, 3.4B, 3.5B, 3.6B, 3.6C), across increment and decrement detection. Thus, clearly, the results aren't as strongly asymmetric as the center-surround theory would suggest. However, there is still room to probe for asymmetries in the data which is consistent with center-surround receptive fields. Every surround/test-pulse configuration in Experiments 1–3 simultaneously measured the increment threshold and decrement threshold. In this analysis section, those paired thresholds are compared and asymmetries are confirmed. These asymmetries particularly for the dark surround are indeed consistent with center-surround receptive fields.

In Experiment 1, over the spatial ranges where peripheral detection are not a concern (36 minutes of arc and wider), the dark surround uniformly raises increment thresholds more than it raises decrement thresholds (Figure 3.8A, blue curves). Moreover, this asymmetry with the dark surround is robust to edge manipulations. Under both edge manipulations introduced in Experiments 2 and 3, the asymmetry in how the dark surround modulates increment and decrement detection remains robust (Figure 3.8B, 3.8C, 3.8D). Thus, regardless of edge-configuration, there is evidence that the dark surround is indeed exciting the OFF surround of an ON cell-type and therefore raising it's threshold even higher.

One would hypothesize that with the light surround decrement threshold would be raised more, however, this could not be robustly concluded from the data (Figure 3.8A). When edge manipulations are introduced there is some inconsistent evidence of an asymmetry, but the results are largely mixed and not as robust as the asymmetries with the dark surround.

3.4 Discussion

Novel Monotonicity

The monotonicity demonstrated both with the light surround in Experiment 1 (Figure 3.4A) and the dark surround with zero-flux test-pulse (Figure 3.7B) are both novel critiques of the crux of the classic linking hypothesis, relating the the bi-phasic Westheimer curve with center-surround receptive field organization. Alternative theories to the Westheimer curve, such as a cortical edge effect or fixational eye-movements, tend to be mono-phasic in nature and their failure to replicate the bi-phasic curve has probably contributed to the duration of the original center-surround linking hypothesis. The monotonicity demonstrated here, and in particular the ability to change the Westheimer curve with the dark surround from bi-phasic to monotonic by adjusting the net photon-flux of the test-pulse (Figure 3.7) leads the author to alternative more mundane explanation of stray light detection by neuron's in the periphery.

Failure of Previous Models and Conjecturing A New model

The combined results of Experiments 1–3, strongly indicate that neither the center-surround hypothesis, nor edge effects, nor their combination are sufficient to explain the observed data when all four polarities of the Westheimer curve are generated. This finding is notable, since the majority of the discussion of the Westheimer curves have revolved around these two hypotheses.

There are a multitude of ways in which an additional theory could be overlaid to "explain" the qualitative nature of the results of Experiments 1–3. One theory is to claim that a simple compressive non-linearity used to describe the cell's response function in

Figure 3.1D is incorrect. Rather than a compressive function, the response function could be sigmoidal in nature. Under this hypothesis increasing and decreasing excitation levels would both lead to less steep portions of the response curve and an increased test-pulse detection thresholds. This could theoretically explain the observed results, while preserving center-surround theories. However, a sigmoidal response curve is largely hypothetical and does not agree with well-established phenomena such as Weber's law. Another theory would be to imply the existence of a hypothetical surround contrast detector which would raise thresholds regardless of polarity of the surround and test-pulse. However, combining this with classic center-surround leads to a theory that is essentially irrefutable. The authors prefer to leave these findings as an implication that neither center-surround nor edge effects are a sufficient explanation.

Functional finding of robust asymmetry

Independent of the Westheimer curves, this experiment also demonstrates that lowering the luminance of a surrounding visual area can preferentially decrease sensitivity of increment detection with less sensitivity loss to decrement detection. This finding itself has potential as a tool for future vision research. The previous manipulation to preferentially decrease the sensitivity of increment detection involved pre-adapting to an intense full-screen ramping stimulus (Krauskopf1980 [4]). While both methods are effective, the current manipulation is preferable due to its temporal stability. First, the manipulation is tonic and does not rely on an effect which decays with time. Moreover, the order of the induced asymmetry are both in the .25 to .50 log units range. Finally, due to the unidirectional nature of the manipulation, the neural source (likely to be center-surround) is easier to identify.

Recent findings in rodent models of glaucoma indicate selective damage to OFF pathway retina ganglion cells in the early stages of glaucoma (El-Danaf2015 [2]). It follows that a visual test which can parse ON and OFF pathways could be useful in the development of an early diagnostic. The psychophysical observations in this paper (Figure 3.8) have potential to generate a host of test-statistics which could indicate a diseased patient.

3.5 Figures

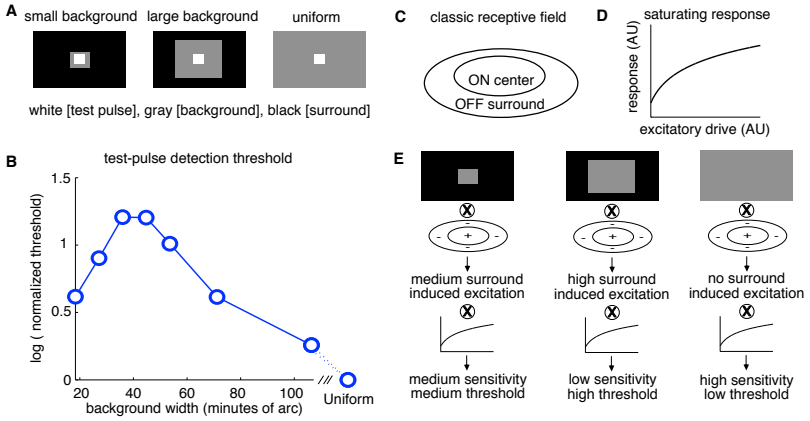

Figure 3.1: **Westheimer Curve**. **A. The Experimental Paradigm:** The detection threshold of a small test-pulse of light (white dot) over a gray background overlayed on a dark surround is compared for different background sizes. **B. Sample Westheimer curve:** The luminance threshold for detecting a small incremental test-pulse of light over a gray background is dependent on the size of the background. If the background covers the whole screen ("uniform" in the plot) the threshold for detection is minimized. As the background shrinks and is replaced by a dark surround, the threshold steadily increases. However, once the background becomes too small ($\sim$ 36 minutes of arc in the above plot), the threshold for detecting a small incremental test-pulse begins to decrease. Thresholds are all normalized by the threshold for detection over a uniform background. **C. Center-Surround of Theoretical Visual Neuron:** Threshold for increment detection is thought to be mediated by ON-type visual neurons with classic center-surround organization and hence an "ON center and OFF surround". **D. Saturating Response of Theoretical Visual Neuron:** Neurons are generally thought of as having a saturating response to excitatory drive. Steeper sections of the curve indicate higher sensitivity. **E. Linking Hypothesis:** Observed Westheimer curve is phenomenologically consistent with an adaptive center-surround detector with saturating responses in the following manner. For a uniform background, the cell receives no tonic excitation the response lies at a steep section, hence the neuron is sensitive and the threshold is low (right column). As the background shrinks the dark surround begins to excite the Visual Neuron's OFF surround, the response slope becomes less steep, hence the detector is less sensitive and the threshold is raised (middle column). Finally the dark surround begins to encroach on the neuron's center, inhibiting the neuron, driving the neuron to a more sensitive regime and hence lowering the threshold again (left column).

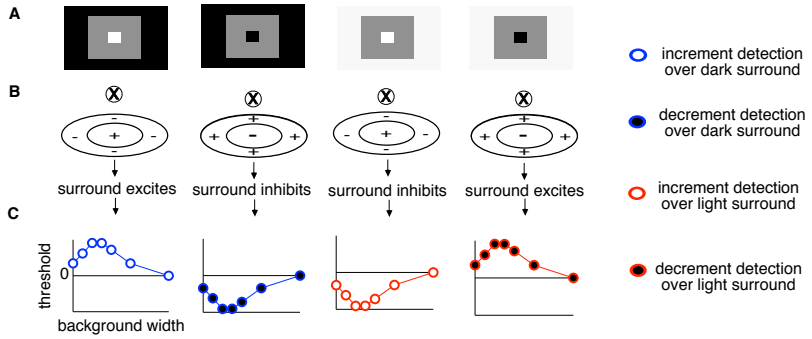

Figure 3.2: **Theory of the Experiment**. **A. Surround and Test-Pulse Polarities:** In addition to the classic Westheimer curve (dark surround with incremental test-pulses), the study explores from left to right, dark surrounds with decremental test-pulses, light surround with incremental test-pulses, and light surround with decremental test-pulses. **B. Detecting Pathway and Surround Effect:** Light increment detection theoretically mediated by ON cells (+ center, − surround). Light decrement detection theoretically mediated by OFF cells (− center, + surround). Dark surrounds excite ON cells while inhibiting OFF cells. Light surrounds inhibit ON cells while exciting off surrounds. **C. Theoretical result of varying background span:** Extrapolating the classic center-surround theory for the Westheimer curve (Figure 3.1E) to the three other stimulus configurations should result in two inverted curves (decrement detection over dark surrounds, increment detection over light surrounds) as well as an OFF analogue to the Westheimer curve (decrement detection over light surround). For the remainder of the document, (blue, red) will denote (dark surround, light surround) and (white dot, black dot) denotes (incremental test-pulse, decremental test-pulse).

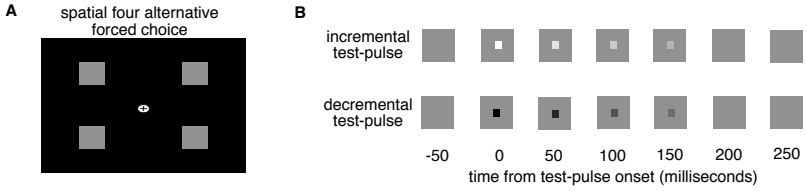

Figure 3.3: **Stimulus Schematic**. **A. Spatial Arrangement:** This schematic shows the tonic background present for detecting test-pulses with a dark surround. A fixation point is present to which subjects foveate. The center of each gray background is symmetrically located in each quadrant, centered at ~ 8 degrees in the periphery. Spatial configuration is identical with the light surround. **B. Test-pulse:** Test-pulses occur randomly in one of the four quadrants in the center of the gray background. Incremental and decremental test-pulse trials are randomly interwoven. The pulses are linear ramps with a 200 millisecond decay duration.

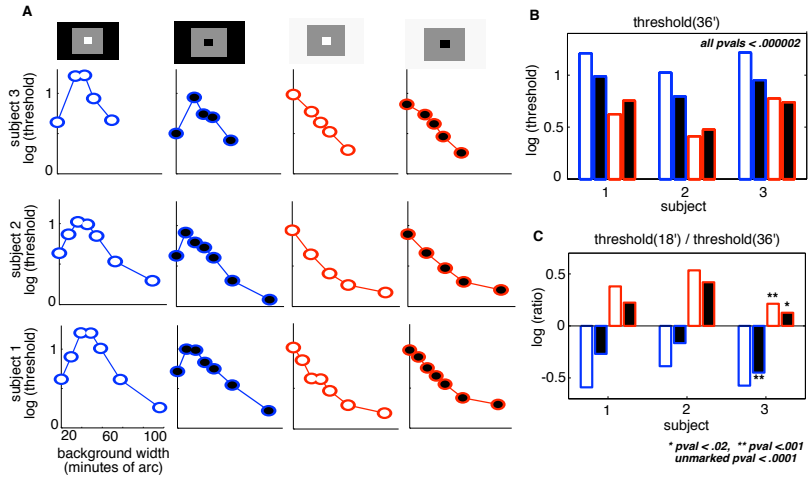

Figure 3.4: **Results of Experiment**. **A. Normalized Detection Thresholds:** Detection thresholds over the four conditions (columns 1-4) and three subjects (Rows 1-3) over all four stimulus polarity configurations. All thresholds are normalized by detection threshold with a uniform background. All axes are identical, test-pulse width was $\sim$ 18 minutes of arc. Note large deviation from theoretical expectations (Figure 3.2C). All normalized thresholds were greater than 0 with p-values $< .001$ (single exception [subject 2, column 2, width 100'] had a p-value of .05). **B. Uniformly Positive Thresholds at 36':** Thresholds are uniformly raised calling into question the neural detector argument. At a background width of 36' (the peak the classic Westheimer curve). All four conditions are uniformly positive with p-values $< .000002$. **C. Bi-phasic Check:** Bi-phasic Westheimer curves were not seen for the light surround, contradicting the center-surround linking hypothesis. Positive values of (threshold(18')/threshold(36')) indicate monotonicity.

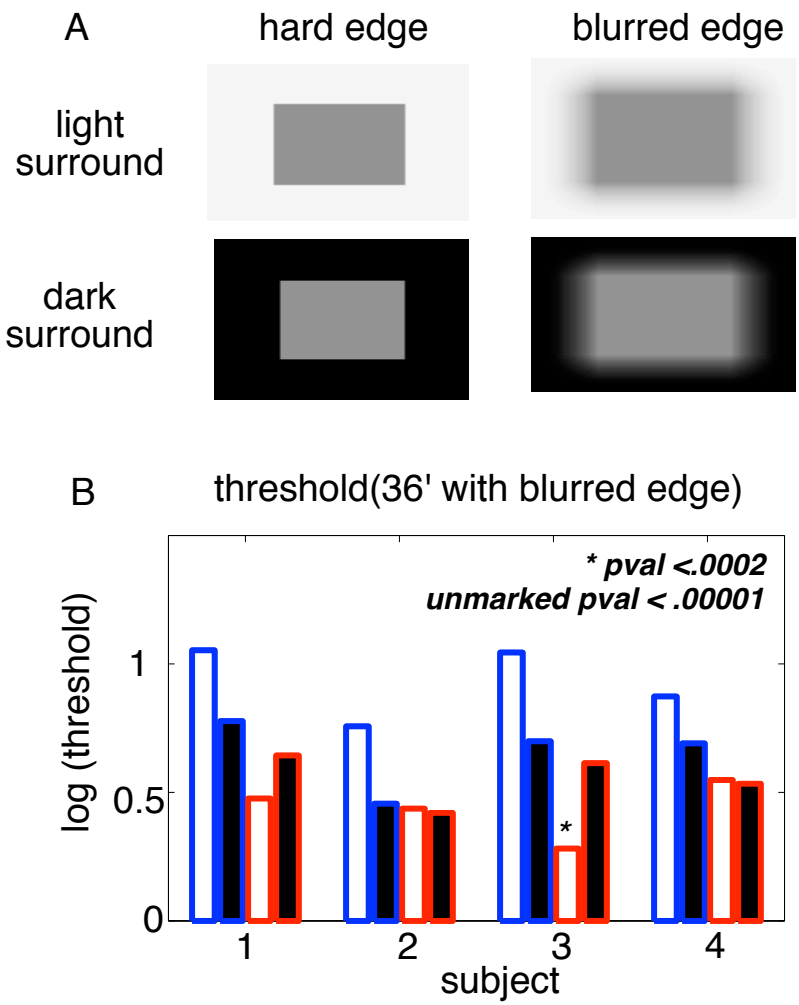

Figure 3.5: **Blurred Edge**. **A. Edge Schematic:** The edge was blurred by using a $\sim 18'$ linear gradient from background to surround. This is contrasted with the hard edge used in experiment 1. **B. Uniformly Positive Thresholds:** Thresholds are uniformly raised with a background width of 36' and a blurred edge, all p-values $< .0002$. Qualitatively comparable to Figure 3.4B.

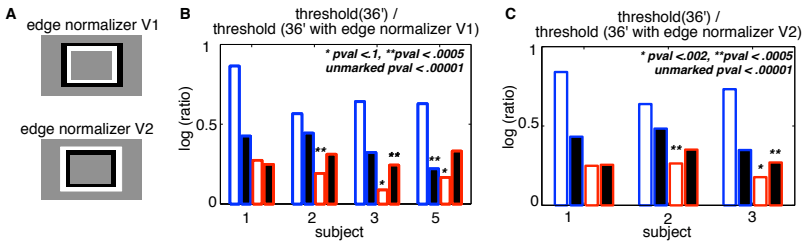

Figure 3.6: **Mod Double Edge**. **A. Schematic of Normalizing Backgrounds:** Threshold detection over gray background with double rings. Each ring width is roughly 4.5', the width of the inner ring is 36'. Both polarities were examined. **B. Uniformly Positive Thresholds:** Thresholds are uniformly raised when normalized by increment/decrement detection over gray background with double rings (white inside, black outside). Together with Figure 3.5, strongly indicates that combination of center-surround and edge effects are insufficient to explain data. **C. Uniformly Positive Thresholds:** Same as Figure 3.6B, but double rings flipped (black inside, white outside).

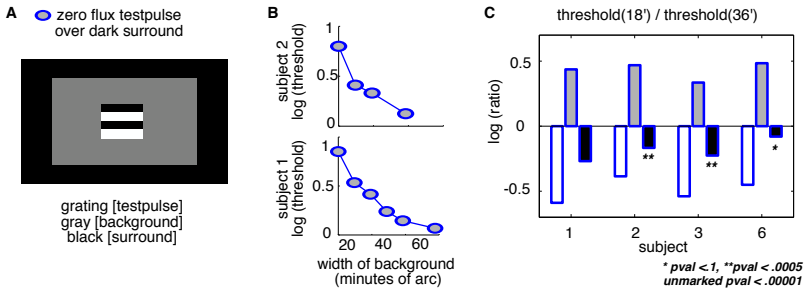

Figure 3.7: **Zero Flux Detection**. **A. Schematic of Zero Flux Test-Pulse:** New test-pulse is a four-row horizontal grating of alternating stripes. The total size is identical to previously used incremental and decremental test-pulse. The average photon flux of the test-pulse is identical to the background. **B. Monotonic rather than Bi-Phasic:** Over a dark-surround, the zero-flux test-pulse detection threshold increases monotonically as the width of the background decreases. Compare with bi-phasic nature of increment/decrement detection over dark surround (Figure 3.4A). **C. Bi-phasic Check:** Analogous to Figure 3.4C, positive numbers indicate monotonic, negative ratios indicate bi-phasic. Zero flux test-pulse clearly has monotonic relationship (p-values $< .00001$).

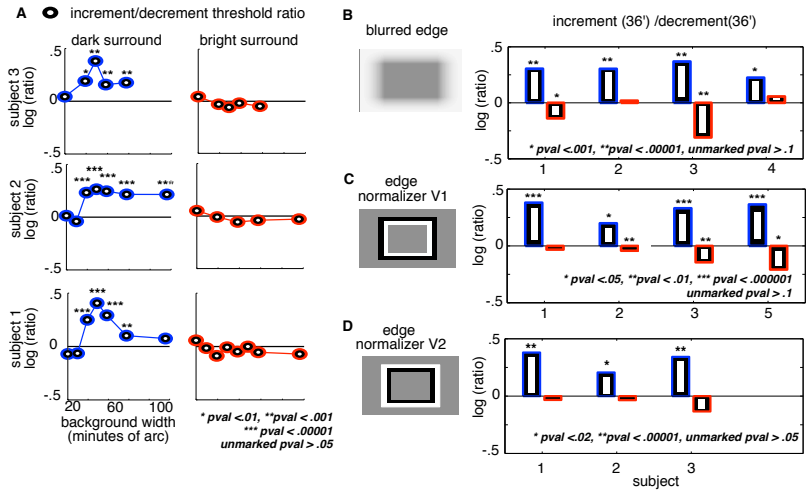

Figure 3.8: **Analysis of Increment Decrement Ratios**. **A. Asymmetry in the Westheimer Curves:** Comparing increment and decrement thresholds of the four Westheimer curves (Experiment 1, Figure 3.4A). The dark surround clearly induces higher increment thresholds than decrement thresholds at background widths of 36' to 60'. No such asymmetry exists with the light surround. **B. Asymmetry is robust to edge blurring:** Comparison of increment and decrement thresholds with a blurred edge (Experiment 2, Figure 3.5B). With the dark surround, the asymmetry is still present. Results are mixed with the light surround. **C. Asymmetry is robust to edge normalization:** Comparing increment and decrement thresholds after normalization by an estimate of the edge effect (Experiment 3, Figure 3.6B). With the dark surround, the asymmetry is still present. Results are mixed with the light surround. **D. Asymmetry is robust to edge normalization:** Comparing increment and decrement thresholds after normalization by an alternate estimate of the edge effect (Experiment 3, Figure 3.6C). With the dark surround, the asymmetry is still present. Results are mixed with the light surround.

References

[1] Crawford, B. H. (1940). The effect of field size and pattern on the change of visual sensitivity with time. *Proceedings of the Royal Society of London B: Biological Sciences, 129*(854), 94-106.

[2] El-Danaf, R. N., & Huberman, A. D. (2015). Characteristic patterns of dendritic remodeling in early-stage glaucoma: evidence from genetically identified retinal ganglion cell types. *The Journal of Neuroscience, 35*(6), 2329-2343.

[3] Kass, R. E., & Raftery, A. E. (1995). Bayes factors. *Journal of the American Statistical Association, 90*(430), 773-795.

[4] Krauskopf, J. (1980). Discrimination and detection of changes in luminance. *Vision Research, 20*(8), 671-677.

[5] Kunken, J. M., Sun, H., & Lee, B. B. (2005). Macaque ganglion cells, light adaptation, and the Westheimer paradigm. *Vision Research, 45*(3), 329-341.

[6] Lennie, P., & MacLeod, D. I. A. (1973). Background configuration and rod threshold. *The Journal of Physiology*, 233(1), 143156.

[7] MacLeod, D. I. A. (1978). Visual sensitivity. *Annual Review of Psychology,29*(1), 613-645.

[8] Sinai, M. J., Essock, E. A., & McCarley, J. S. (1999). Spatial sensitization of increments and decrements: a border-contrast process and a net-excitation process. *Vision Research, 39*(10), 1847-1860.

[9] Schiller, P. H., Sandell, J. H., & Maunsell, J. H. (1986). Functions of the ON and OFF channels of the visual system. *Nature, 322*, 824825

[10] Westheimer, G. (1965). Spatial interaction in the human retina during scotopic vision. *The Journal of Physiology, 181*(4), 881-894.

[11] Westheimer, G. (1967). Spatial interaction in human cone vision. *The Journal of Physiology, 190*(1), 139154.

[12] Westheimer, G. (2004). Center-surround antagonism in spatial vision: Retinal or cortical locus? *Vision Research, 44*(21), 2457-2465.

[13] Wilks, S. S. (1938). The large-sample distribution of the likelihood ratio for testing composite hypotheses. *The Annals of Mathematical Statistics, 9*(1), 60-62.

This chapter presents the main material for the following manuscript:

Heitman, Alexander K.; MacLeod, Donald I.A. "Analyzing stimulus polarity configurations to examine neural factors underlying the Westheimer effect in peripheral vision".

The manuscript is in the final stage of preparation and will be submitted soon. The journal is still undecided. Alexander Heitman is the primary researcher of the manuscript and conducted the majority of the experiments, data analysis, and writing. Dr. Don MacLeod was instrumental in conceptualizing the project and wrote the code for the stimulus staircase as well as the sigmoidal curve fitting. The author is very thankful for the support provided by Dr. MacLeod throughout the entire process.

Chapter 4

Recurrent suppression in ON parasol retinal ganglion cells

4.1 Abstract

A major challenge in understanding the function of neural circuits is the role of modulatory networks. Here we demonstrate that recurrent response suppression shapes early visual signals in the magnocellular visual pathway in the primate. Using an indirect electrical imaging method, we identify a type of polyaxonal amacrine cell that are gap junction coupled to ON-parasol (magnocellular-projecting) retinal ganglion cells. Coupling causes the amacrine cells to fire spikes that propagate over long distances, producing GABA-ergic inhibition of other ON-parasol cells. These PACs closely mirror the activity of the ON parasol cells and transmit these over several millimeters and inhibit ON parasol cells along the axon. We propose a model by which the extra-classical receptive field of the ON parasol cells is not formed by feedforward inhibition from a independent cell type, but rather by reciprocal inhibition from the ON parasol cells in the periphery themselves via an electrically coupled PAC.

4.2 Significance Statement

Using an indirect electrical imaging technique, we found a amacrine subcircuit that recurrently modulates the activity of retinal ganglion cells in the magnocellular visual pathway, which feeds the most extensively studied visual areas in the primate brain. The amacrine cells are electrically coupled to ON-parasol cells and propagate their activity actively over long distances, producing inhibition of ON-parasol cells in their periphery. This implies that the extra-classical receptive field of ON-parasol cells is partly formed by the ganglion cells themselves instead of being separately constructed through feedforward inhibition. Since every cell receives inhibition via the amacrine cells from a larger number of distant cells this kind of response normalization should reflect precisely the mean population activity.

4.3 Introduction

A major feature of visual processing in the brain is recurrent response normalization, which accounts for diverse aspects of modulation of light responses outside of the classical receptive field (Heeger1992 [10], Carandini1997 [2]). In the retina, extra-classical receptive field effects have long been observed (McIlwain1964 [17], Levick1965 [13], Werblin1972 [25], Passaglia2001 [19], Zaghloul2007 [26], Baccus2008 [1], Olveczky2003 [18], Hoggarth2015 [11]). Ganglion cells collect visual information over the receptive field in which an excitatory center region is compared to an inhibitory surround. In several ganglion cell types, their activity can be modulated by stimuli outside this classic receptive field. This extra-classical receptive field can extend over several millimeters over the retinal surface.

An important retinal cell class with the appropriate connectivity to perform recurrent normalization is the amacrine cells – the most diverse and least understood cell class in the retina, constituting at least 25 different types distinguished by morphology, connectivity to specific bipolar and ganglion cell types, and neurotransmitters (see Masland2012 [16]). Very few amacrine cell types have been isolated and recorded electrically because of their

limited accessibility.

Recently, we characterized polyaxonal amacrine cell (PAC) types in the primate retina (Greschner2014 [8]). However, we could not find any interaction of these types with one of the major ganglion cell type in the primate retina. Here we used the spike-triggered electrical activity (electrical image) to screen for temporally precise interactions between cells. Previous studies have shown that specific amacrine cell types are electrically coupled to specific retinal ganglion cell types (e.g. Marc2002 [15], Völgyi2009 [24]). We exploited this fact to target and characterize a previously unrecorded amacrine cell type that is electrically coupled to ON-parasol ganglion cells in primate retina (Dacey1992 [5], Jacoby1996 [12]). ON-parasol cells are frequently sampled in extracellular recordings (Field2007 [6]) and subserve one of the major retino-geniculate visual pathways (Perry1984 [20]). We found that ON parasol cells are electrically coupled to a, up to now unrecorded PAC type. These PACs closely mirror the activity of the ON parasol cells and transmit these over several millimeters and inhibit ON parasol cells along the axon. We propose a model by which the extra-classical receptive field of the ON parasol cells is not formed by feedforward inhibition from a separate cell type, but rather at least partly by reciprocal inhibition from the ON parasol cells in the periphery themselves via an electrically coupled PAC.

4.4 Materials and Methods

Retinas were obtained and recorded as described previously (Litke2004 [14], Frechette2005 [7]). Briefly, eyes were taken from terminally anesthetized macaque monkeys (Macaca mulatta, M. fascicularis), used by other laboratories in the course of their experiments, in accordance with institutional guidelines for the care and use of animals. Segments of peripheral retina were isolated from the pigment epithelium, and placed flat, ganglion cell side down, on a planar array of extracellular microelectrodes. Two different electrode arrays of 512 electrodes were used. One array covered a rectangular region $1890 \times 900\,\mu m$, the second a hexagonal region $3120\,\mu m$ wide. While recording, the retina

was perfused with Ames' solution ($33-36°C$) bubbled with 95% O_2 and 5% CO_2, pH 7.4.

Recordings were analyzed off-line to isolate the spikes of different cells, as described previously (Frechette2005 [7], Field2007 [6]). Briefly, candidate spike events were detected using a threshold on each electrode, and the voltage waveforms on the electrode and neighboring electrodes around the time of the spike were extracted. Clusters of similar spike waveforms were identified as candidate neurons if they exhibited a refractory period. Duplicate recordings of the same cell were identified by temporal cross-correlation and removed.

A white noise stimulus, composed of a lattice of square pixels updating randomly and independently of one another over time, was used to characterize the spatial, temporal, and chromatic response properties of recorded cells (Chichilnisky2001 [3]). The spike-triggered average stimulus obtained in response to white noise was taken as a summary of the spatio-temporal-chromatic light response properties of the cell. The receptive fields were summarized by fitting the STA with a two-dimensional elliptical Gaussian function. These receptive fields fits were visualized by an ellipse for each cell representing the 1 SD contour of the Gaussian (Figure 4.1A). Correspondences between functionally defined ganglion cell types, and previously identified morphologically distinct ganglion cell types (e.g. ON-parasol) were inferred based on cell densities and light response properties (Field2007 [6]).

To evaluate the effects of gap junction blocker meclofenamic acid (Sigma; Figure 4.2A), changes in amplitude of the electrical image of axonal spikes between control, drug and washout conditions were measured. Meclofenamic acid was used in a low concentration ($20\,\mu M$) to enable a washout. At higher concentrations ($100\,\mu M$), PAC axons were no longer detected, but the long-term stability of the recording was not sufficient to reverse the observed effects after a washout.

Electrical images were calculated as the spike-triggered average electrical signal across the array for each cell separately (Litke2004 [14], Petrusca2007 [21], Greschner2014 [8]). Specifically, for each electrode, the voltage waveform during the time period from $0.5\,ms$ before to several milliseconds after each spike from the cell was identified, and the average

across spikes was computed. To display the electrical image, the minimum voltage deflection at each electrode was shown using the spatial layout of the electrodes, represented by the size of disk and its gray value. Largest amplitudes were saturated to increase visibility of PAC axons. The conduction velocity of action potentials in ON parasol cells and PAC axons (Figure 4.3) was estimated by a linear fit to the distance the spike traveled along the axon per unit time.

Cross-correlation functions (Figure 4.4 B–F) were obtained by binning spikes into $1\,ms$ time bins and computing the correlation coefficient between the resulting spike count vectors, as a function of temporal offset. ON-parasol cells were classified manually into groups that did, and did not, overlap with a PAC axon. ON-parasol cells very near to the reference cell were omitted, because they exhibited strong positive correlations from shared photoreceptor noise and electrical coupling (Trong2008 [23], Greschner2011 [9]).

To estimate how response suppression by PACs modulates visual signals, a generalized linear model (GLM) was fitted to the data (Figure 4.5B). The GLM consists of a bias term μ, stimulus filter k, a spike-history filter h, and a set of incoming coupling filters $\{l_i\}$. The parameters act on the stimulus x, the spike train of the fitted neuron y, and the spike trains of other RGCs that could affect that firing rate of the fitted neuron $\{y_i\}$.

$$\lambda(t) = \exp(\mu + k \cdot x(t) + h \cdot y(t) + \{l_i\} \cdot \{y_i\}). \tag{4.1}$$

The convex nature of the maximum likelihood estimator for the GLM guarantees that the optimal model fit is found (Pillow2008 [22]).

A GLM (μ, k, h, l) was fitted to ON parasol cells one PAC at a time in the presence of a white noise stimulus. Strong coupling filters $\{l_i\}$ were found in over thirty cells across three different retinas (Figure 4.5C). The significant difference between the average coupling filter of cells which and did not intersected PAC axons (Figure 4.5D) was verified for five PACs across two different retinas.

Center-surround gratings were presented to probe the function of the proposed inhibitory PAC circuit (Figure 4.6B). Six different spatial frequencies were used in the

center and eight different spatial frequencies and a uniform gray were used in the surround. Each combination was shown for $10-12$ seconds in a randomized order, and repeated two to three times. Each center suppression profile (gray line) was normalized by the center spike rate while a uniform gray was presented in the surround. The black average line is a standard uniformly weighted average of the center suppression profiles.

A GLM (μ, k, h) was fit to the white noise stimulus for all cells which were used in Figure 4.6B. A strong representative PAC coupling filter lrep with a gain loss of 15% was used to simulate PAC inhibition. Each cell then had 2 free scaling parameters ($c_1 * \mu$, $c_2 * k$, h, l_{rep}) to refit the GLM to the drifting grating stimulus. The parameters c_1 and c_2 were fit to minimize the square difference between the observed frequency tuning curve and the GLM simulated tuning curve. Using the refitted GLM we then simulated all of the center cell models with the same stimulus conditions and durations which were used in the experiment. Surround inhibition was modeled as a Poisson process with frequency determined by the measured firing rate of surround cells (Figure 4.6A) multiplied by the simulated number of PACs assumed to converge onto the ON-parasol cell.

4.5 Results

To screen for possible interaction partners of parasol cells, their electrical signatures were analyzed in large-scale multi-electrode recordings. From voltage recordings on a high-density 512−electrode array, the spikes of hundreds of recorded cells of several types were sorted on the basis of their characteristic spatio-temporal waveforms (Litke2004 [14], Frechette2005 [7]) (see Methods 4.4). Parasol cells were identified by their characteristic density and light responses (Frechette2005 [7], Field2007 [6]). Then, using all the spike times of a given parasol cell, the average voltage waveform over all electrodes near the time of the spike was calculated (Litke2004 [14], Petrusca2007 [21], Greschner2014 [8]) (Figure 4.1 B–D). This electrical image revealed the average spatiotemporal pattern of voltage deflections recorded over the array during and after the occurrence of the parasol cell spike. The averaging procedure made it possible to detect and characterize small

voltage deflections far from the soma.

As expected from previous work (Litke2004 [14], Petrusca2007 [21], Greschner2014 [8]), the large biphasic somatic spike produced by the parasol cell was surrounded by a smaller opposite-sign dendritic potential on nearby electrodes, and was followed by a triphasic axonal spike propagating across the array toward the optic disc (Figure 4.1B, C). However, in ON-parasol cells, on closer inspection, the electrical image revealed additional structure. In addition to the main axonal spike (Figure 4.1C, trace 2), smaller secondary spikes were detected, emanating from a region near the ON-parasol cell soma, and propagating simultaneously, and more slowly, in multiple directions (Figure 4.1C, traces 3-7) (see supplementary movie 4.7). The electrical image of the ON-parasol cell and the auxiliary spike axons can be separated in time (Figure 4.1D). This pattern of radial spike propagation, in some cases over $3\,mm$ (max. distance observable on the multi-electrode array), is consistent with only one known cell class in the retina: spiking polyaxonal amacrine cells (PACs) (Greschner2014 [8]). These auxiliary spikes were present in recordings of both spontaneous and visually driven activity.

Why would recordings from an ON-parasol cell reveal the superimposed electrical signature of a PAC? Spike sorting artifacts were unlikely, given the discrete clusters formed by the parasol cell spike waveforms and the fact that these additional PAC spikes were observed only in ON-parasol cells. The most likely origin of these signatures is electrical coupling: because the electrical image is calculated by averaging voltage waveforms recorded at the times of ON-parasol cell spikes, voltage fluctuations in any cell that fires in a precise temporal relationship to the ON-parasol cell, will appear in the electrical image. Previous anatomical work has revealed a type of PAC tracer-coupled, and thus presumably electrically coupled, to ON-parasol cells (Dacey1992 [5], Jacoby1996 [12]). Strong electrical coupling would be expected to produce spikes in these PACs in a precise temporal relationship to spikes in the ON-parasol cell. Based on these considerations, the auxiliary axons in electrical images were interpreted as revealing spikes from PACs electrically coupled to parasol cells.

The interpretation that the auxiliary axons originate from electrically coupled

PACs was supported by blockade of gap junction coupling using meclofenamic acid (Figure 4.2A). It reduced the magnitude of auxiliary axon signals in the electrical image relative to the strength of the primary axon signal. Since the electrical image is the average voltage waveform around the time of a somatic spike of the reference cell, this can be interpreted as reduced coupling of the PAC and the ON-parasol cell and therefore fires less frequently synchronously. Gap junctions are commonly found between various cell types in the retina and the effects of gap junction blockers are generally hard to interpret. However, in this case, the electrical image allows to separately analyze the coupling of the ON parasol cell and the PAC. Furthermore, the reduction of strength in the electrical image would not be expected from an overall suppression of firing by the drug, but would be expected based on reduced coupling of two cells. A concentration of $100\,\mu M$ meclofenamic acid led to the complete disappearance of the auxiliary axon signals and could be interpreted as a complete uncoupling of the ON parasol cell and PAC. However, a recovery after wash-out was in this case only achieved with a concentration of $20\,\mu M$, which led to an incomplete reduction.

The number of ON parasol cells which displayed detected PAC axons was variable across preparations. In some cases PAC axons could be detected on over 90% of ON parasol cells. The largest PAC axonal spikes were up to 10% of the amplitude of ON parasol axonal spikes. Examining the distribution of voltage amplitudes at the electrodes that show PAC axons can give a rough estimate of the reliability of electrical coupling. If every ON-parasol spike triggered a PAC spike, the voltage distribution at an electrode should be unimodal, whereas unreliable coupling would be expected to produce a distribution composed of voltages recorded with and without PAC spikes. The observed distribution can be modeled using variance from other portions of the voltage trace (Figure 4.2B). The estimated coupling efficiencies varied from cell to cell (57%, $\pm 17\%\,SD$; 61 ON-parasol cells).

Furthermore, in agreement with earlier results from different types of PACs, that were directly recorded (Greschner2014 [8]) the spike conduction velocity of PAC axons was much slower than that of the ON-parasol axon ($0.5m/s$, $\pm 0.1\,SD$; $1.5m/s$, $\pm 0.2\,SD$;

28 cells) (Figure 4.3A). As in other PAC types, spike conduction velocity declined as a function of distance from the soma, unlike in ON-parasol cell axons. To analyze the conduction velocity, the timing of axon spikes was examined as a function of distance (Figure 4.3B). This also revealed a delay between the ON-parasol cell spike and the PAC spike initiation, suggesting that the parasol cell spike predominantly caused the PAC spike.

Many types of amacrine cells, including PACs, are known to exert an inhibitory influence on retinal ganglion cells (Masland2012 [16]). To test whether firing of this PAC type modulated the firing of simultaneously recorded ganglion cell types, the spike times of the PAC, were inferred from spike times of the original ON-parasol cell. In recordings of spontaneous activity, the spike times of the PAC were correlated with the spikes of ganglion cells. For ON parasol cells, the correlation analysis of spontaneous activity revealed a spatially specific pattern of interaction with the PAC (Figure 4.4A). On average, the ON-parasol cells lying near the axons of the PAC exhibited reduced firing after the occurrence of an inferred PAC spike, while parasol cells farther from the axons did not (Figure 4.4C, D), suggesting that the PAC provided inhibitory synaptic input to other ON-parasol cells. This interpretation was supported by blockade with the GABAA receptor antagonist gabazine ($5\,\mu M$) (Figure 4.4E, F). In sum, these findings are consistent with the hypothesis that PACs are electrically coupled to ON-parasols near the ON-parasol cell soma, and form GABA-ergic synapses with other ON-parasol cells along their axons (Figure 4.5A) (Jacoby1996 [12]).

How does response suppression by PACs modulate visual signals transmitted to the brain by the ON-parasol cells? This was quantified by analyzing modulation of ON-parasol cell firing in the presence of a white noise visual stimulus. To tease apart the effects of the visual stimulus and PAC inhibition, a generalized linear model (GLM) was fitted to the recorded responses (Pillow2008 [22]). In the GLM, stimulus driven responses sum with spike driven feedback from other cells to drive spikes via a nonlinear mechanism (Figure 4.5B). The spatiotemporal light sensitivity of the GLM, and the sign and time course of the spike dependent feedback, were fitted to data. Sample fits (Figure 4.5C) show that feedback associated with PAC spikes suppressed ON-parasol firing in the presence of the

stimulus, with a time course similar to suppression observed with no stimulus (Figure 4.4B). The coupling filter of PACs to ON-parasol cells lying near their axons were suppressive on average across cells, while those of non-overlapping cells were not (Figure 4.5D). Thus, response suppression by PACs is likely to modulate visual signaling in ON-parasol cells.

To assess the spatial structure of PAC response suppression, the retina was stimulated with a central modulating sinusoidal grating pattern surrounded by a larger modulating background grating (McIlwain1964 [17], Levick1965 [13], Werblin1972 [25], Passaglia2001 [19], Olveczky2003 [18], Zaghloul2007 [26], Baccus2008 [1]). Responses of ON-parasol cells with receptive fields in the central region exhibited suppression by the surround stimulus. A possible origin of this suppression is lateral inhibition in the ON-parasol network: the firing of an ON-parasol cell is suppressed by multiple PACs, which are driven by excitation of surrounding ON-parasol cells. To examine this possibility, the excitatory tuning of ON-parasol cells to sinusoidal gratings was compared to the tuning of PAC-mediated suppression. ON-parasol cells stimulated with sinusoidal gratings exhibited an excitatory frequency tuning that peaked at 0.38–0.77 cpd (Figure 4.6A, 3 retinas). Introduction of a surround grating suppressed firing of central ON-parasol cells, with maximum response suppression occurring at frequencies similar to the peak excitatory tuning (Figure 4.6B, 0.38–0.77 cpd, 3 retinas). The similarity between ON-parasol excitatory frequency tuning and surround suppression is consistent with recurrent lateral inhibition mediated by PACs. To further test the hypothesis, a re-fitted GLM (see Methods 4.4) was used to predict responses to the same combinations of central and peripheral modulating gratings. By using a strong representative PAC coupling filter in the model a rough, upper bound estimate of the number of surrounding PACs a given ON-parasol cell receives a suppressive signal from (55, 52, 16; 3 retinas). This modeling approach reproduced the frequency tuning of surround suppression (Figure 4.6C), consistent with an origin in PACs electrically coupled to remote ON-parasol cells.

4.6 Discussion

The indirect electrical imaging method revealed the recurrent modulatory function of a network of amacrine cells in the primate retina. The electrical coupling from ON-parasol cells to this amacrine cell type, and the consequent suppression of other ON-parasol cells over a large region, implies that a component of the extra-classical receptive field surround is assembled from the recurrent responses of other ON-parasol cells, rather than a distinct network of interneurons. Since every ON-parasol cell receives inhibition via the PACs from multiple distant cells this kind of response normalization should reflect precisely the mean ON-parasol activity.

Among the major cell types (ON midgets, OFF midgets, ON parasol, OFF parasol and small bistratified cells), the ON-parasol cells were the only cell type that showed electrical coupling to an amacrine cell. However, an earlier report studying the tracer coupling between parasol and amacrine cells made no distinction between the coupling pattern of ON and OFF parasol cells (Dacey1992 [5]). It is possible that existing PAC axons in the OFF layers were not picked up by this method. However, the most prominent PAC type in these kind of recordings is a OFF type (Greschner2014 [8]).

As in many experimental studies involving gap junctions, we observed a certain variability of the coupling strength across preparations. This might possibly reflect variations in the adaptive or circadian state of the tissue. Variations of the coupling strength within a preparation possibly reflect variations in the overlap of the ON-parasol cells and the PACs within their respective mosaics. The amount of overlap is likely to translate into in the amount of gap junction coupling. Variations in the timing of the inhibition in the order over $8\,ms$ are due to runtime differences along the several millimeter long axons that are combined with an inhibition lasting roughly $15\,ms$. In summary, every ON-parasol cell receives inhibition reflect a slightly low-pass filtered mean ON-parasol activity.

Similar recurrent normalization of responses is thought to be important for diverse neural computations in visual cortex (see Heeger1992 [10]); the present results indicate that this important neural computation begins in the retina.

4.7 Figures

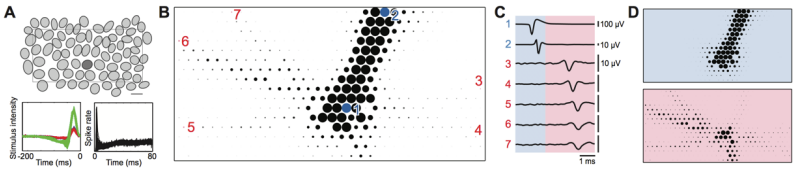

Figure 4.1: **The electrical image of ON-parasol cells reveals unexpected radially propagating axons**. **A.** Mosaic of simultaneously recorded ON-parasol cell receptive fields (top) (scale bar 200 μm), overlaid spike-triggered average response time course (lower left) and autocorrelation of firing (lower right). **B.** Electrical image of a single ON-parasol cell (marked dark gray in A), on the multi-electrode array (32×16 electrodes, 60 μm spacing). Size of disk and gray value represent minimal voltage deflection on each electrode. Largest amplitudes are saturated to increase visibility of PAC axons. **C.** Average voltage traces of electrodes marked in B during a recorded spike in the ON parasol cells, with characteristic somatic (trace 1) and axonal waveforms of ON parasol cell (trace 2) and PAC (trace 3-7). Blue and red regions indicate times before and after a time point 0.85 ms after the largest negative voltage deflection at the soma. **D.** Electrical image before (blue) and after (red) a time point 0.85 ms after minimal voltage deflection, revealing distinct spatial patterns.

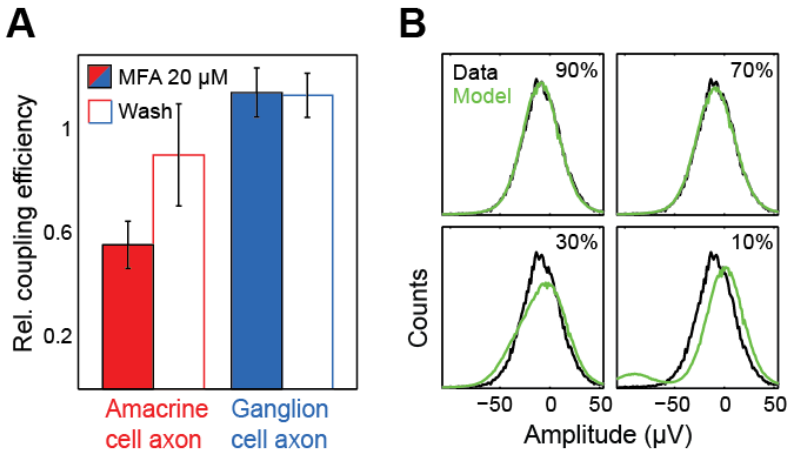

Figure 4.2: **Electrical coupling between ON parasol retinal ganglion cells and polyaxonal amacrine cells (PACs) produces the radial axonal electrical images**. **A.** Estimated coupling strength between ON parasol cells and PACs in the presence and absence of gap junction blocker meclofenamic acid (MFA, 20 μM). Error bars indicate SD over 7 cells. Values are shown relative to the control condition. **B.** Unimodal distribution of voltage values indicates high coupling efficiency between PACs and ON parasol cells. Distribution of peak voltage deflection values on a single electrode along the PAC axon are shown in black. Model prediction for various spiking probabilities while maintaining identical mean amplitude. Best-fitted estimate of observed distribution in H is given by a coupling coefficient (probability of PAC spike given the occurrence of an ON-parasol spike) of 86%.

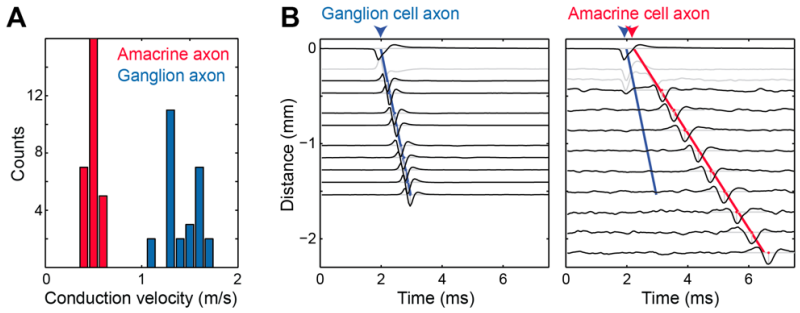

Figure 4.3: **Spike conduction velocity of PAC axons was much slower than that of the ON parasol axon**. **A.** Distribution of conduction velocities of ON-parasol cell axons and PAC axons in a single recording (28 cells). Mean: $1.5m/s \pm 0.2\,SD$, $0.5m/s \pm 0.1\,SD$ respectively. **B.** Voltage waveforms from electrodes obtained at different distances from the soma along the ON-parasol cell and PAC axon. Time of spike initiation at the soma was linearly extrapolated toward zero from axon spike times (ON parasol axon blue line, PAC axon red), resulting in an estimated delay between ON parasol and PAC spike initiation. Dendritic waveforms were not used and are indicated in light gray. Waveform amplitudes are normalized.

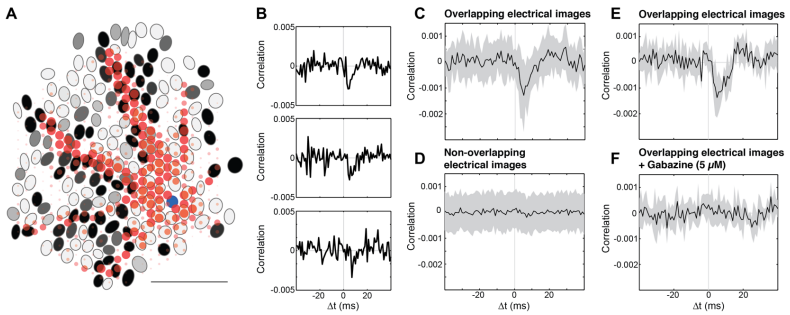

Figure 4.4: **Spontaneous activity of ON parasol cells near PAC axons is suppressed by PAC firing**. **A.** Electrical image of one PAC (red) coupled to one ON-parasol cell (receptive field in blue), aligned with receptive field mosaic of all simultaneously recorded ON parasol cells. Grayscale for ON-parasol cells indicates amplitude of negative correlations of spontaneous activity between that cell and the original ON-parasol cell (minimum observed correlation coefficient $= -0.0042$). Correlations were measured in an $8\,ms$ time interval, shifted according to the conduction time along PAC axon. Electrical image is shown for 2-6 ms after the ON-parasol somatic spike, as in Fig 1D lower panel. Scale bar $1\,mm$. **B.** Cross-correlation function for ON-parasol cells along one axon, sorted by distance from PAC/reference ON-parasol cell soma, revealing deflections suggestive of response suppression. Bin size $1\,ms$. **C, D.** ON parasol cells with somas near and far from the axons of the PAC were suppressed and not, respectively. Near and far ON parasol cells were separated based on their electrical image overlap with the electrical image of the PAC. Traces show cross-correlation functions, averaged across cells after adjustment for conduction time along the PAC axon. Neighboring ON parasol cells exhibited strong positive correlations due to shared input and direct coupling (see Methods 4.4), and thus were excluded from analysis. Bin size $1\,ms$, shaded area 1SD, 18 overlapping, 118 non overlapping cells. **E.** As C, different preparation. Shaded area 1SD, 10 ON parasol cells and one PAC. **F.** Negative correlations blocked by $5\,\mu M$ gabazine (SR-95531). As E. Separate preparations were used for A, B–D and E–F.

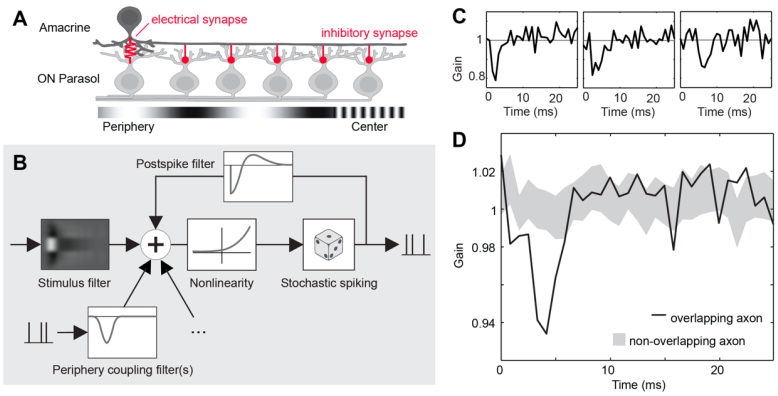

Figure 4.5: **The PAC network recurrently inhibits light responses of ON-parasol cells**. **A.** Schematic model of hypothesized PAC-mediated lateral inhibitory network. **B.** Schematic of the generalized linear model (GLM) used to summarize and analyze light responses and lateral inhibition of ON-parasol cells. The spike rate controlling the model output is a nonlinear function of the sum of the filtered stimulus, filtered spike trains representing inputs from PACs, and a post-spike feedback filter internal to the cell. **C.** Individual fitted coupling filters representing PAC inputs, which modulate the gain of light driven inputs to the modeled ON-parasol cell. All filters were fitted to data obtained in the presence of a white noise stimulus. **D.** Average coupling filter associated with 20 ON-parasol cells overlying PAC axon (dark line) and mean ± SD of filters associated with 20 ON-parasol cells (resampled from ∼ 150 cells) not overlying PAC axon (gray range). Filters adjusted for conduction time along the PAC axon prior averaging. Same preparation as Figure 4.4B–D.

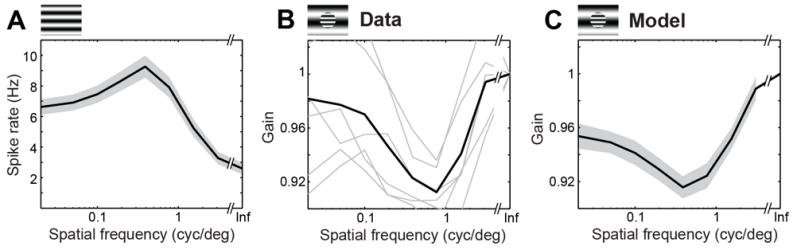

Figure 4.6: **Model of recurrent inhibition reproduces extra classical receptive field effects in ON parasol cells**. **A.** Spatial frequency tuning of ON-parasol cells to full-field sinusoidal drifting gratings (at $4\,Hz$; $n = 89$), shaded region $\pm$ 1 SD. **B.** Normalized response to central grating pattern, as a function of spatial frequency of a surrounding grating pattern (10 degree center diameter). Each gray line represents a specific central grating frequency (0.77, 0.38, 0.19, 0.1, 0.05, 0.02 cyc/deg; at $4\,Hz$); black line represents average ($n = 13$ ON-parasol cells). **C.** Refitted GLM simulations of surround suppression using fits of the model to data from the same cells as in panel F (see Methods 4.4). Insets on top A–C indicate stimulus.

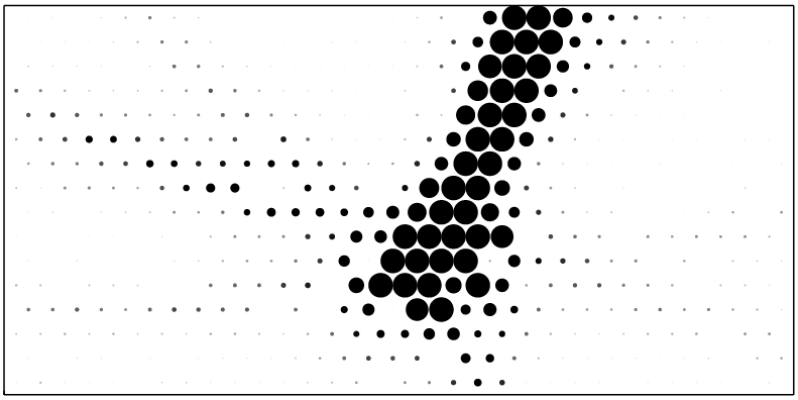

Figure 4.7: Animation of electrical image of cell in Figure 4.1B. Frame duration 0.05 ms, from 0.5 ms before the spike initiation until 5 ms after. Size of disk and saturation represent minimal deflection on each electrode. Largest amplitudes are saturated to increase visibility of PAC axons.

References

[1] Baccus S.A., Olveczky B.P., Manu M., & Meister M. (2008). A retinal circuit that computes object motion. *J Neurosci* 28(27):6807-6817.

[2] Carandini M., Heeger D.J., & Movshon J.A. (1997). Linearity and normalization in simple cells of the macaque primary visual cortex. *J Neurosci* 17:86218644.

[3] Chichilnisky E.J. (2001). A simple white noise analysis of neuronal light responses. *Network* 12:199213.

[4] Chichilnisky E.J., & Kalmar R.S. (2002). Functional asymmetries in ON and OFF ganglion cells of primate retina. *J Neurosci* 22(7):2737-2747.

[5] Dacey D.M., & Brace S. (1992). A coupled network for parasol but not midget ganglion cells in the primate retina. *Vis Neurosci* 9(3-4):279-290.

[6] Field G.D., Sher A., Gauthier J.L., Greschner M., Shlens J., Litke A.M., & Chichilnisky E.J. (2007). Spatial properties and functional organization of small bistratified ganglion cells in primate retina. *J Neurosci* 27(48):13261-13272.

[7] Frechette E.S., Sher A., Grivich M.I., Petrusca D., Litke A.M., & Chichilnisky E.J. (2005). Fidelity of the ensemble code for visual motion in primate retina. *J Neurophysiol* 94(1):119-135.

[8] Greschner M., Field G.D., Li P.H., Schiff M.L., Gauthier J.L., Ahn D., Sher A., Litke A.M., & Chichilnisky E.J. (2014). A polyaxonal amacrine cell population in the primate retina. *J Neurosci* 34(10):3597-3606.

[9] Greschner M., Shlens J., Bakolitsa C., Field G.D., Gauthier J.L., Jepson L.H., Sher A., Litke A.M., & Chichilnisky E.J. (2011). Correlated firing among major ganglion cell types in primate retina. *J Physiol* 589:7586.

[10] Heeger D.J. (1992). Normalization of cell responses in cat striate cortex. *Vis Neurosci* 9:181198.

[11] Hoggarth A., McLaughlin A.J., Ronellenfitch K., Trenholm S., Vasandani R., Sethuramanujam S., Schwab D., Briggman K.L., & Awatramani G.B. (2015). Specific wiring of distinct amacrine cells in the directionally selective retinal circuit permits independent coding of direction and size. *Neuron Apr 8*;86(1):276-91.

[12] Jacoby R., Stafford D., Kouyama N., & Marshak D. (1996). Synaptic inputs to ON parasol ganglion cells in the primate retina. *J Neurosci* 16(24):8041-8056.

[13] Levick W.R., Oyster C.W., & Davis D.L. (1965). Evidence that McIlwain's periphery effect is not a stray light artifact. *J Neurophysiol* 28:555559.

[14] Litke A.M., Bezayiff N., Chichilnisky E.J., Cunningham W., Dabrowski W., Grillo A.A., Grivich M., Grybos P., Hottowy P., & Kachiguine S. (2004). What does the eye tell the brain? Development of a system for the large-scale recording of retinal output activity. *IEEE Trans Nucl Sci* 51:14341440.

[15] Marc R.E., & Jones B.W. (2002). Molecular Phenotyping of Retinal Ganglion Cells. *Journal of Neuroscience* 22(2):413427.

[16] Masland R.H. (2012). The neuronal organization of the retina. *Neuron 76*(2):266-280.

[17] McIlwain J.T. (1964). Receptive fields of optic tract axons and lateral geniculate cells: peripheral extent and barbiturate sensitivity. *J Neurophysiol* 27:11541173.

[18] Olveczky B.P., Baccus S.A., & Meister M. (2003). Segregation of object and background motion in the retina. *Nature* 423:401408.

[19] Passaglia C.L., Enroth-Cugell C., & Troy J.B. (2001). Effects of remote stimulation on the mean firing rate of cat retinal ganglion cells. *J Neurosci* 21:57945803.

[20] Perry V.H., Oehler R., & Cowey A. (1984). Retinal ganglion cells that project to the dorsal lateral geniculate nucleus in the macaque monkey. *Neuroscience* 12(4):1101-1123.

[21] Petrusca D., Grivich M.I., Sher A., Field G.D., Gauthier J.L., Greschner M., Shlens J., Chichilnisky E.J., & Litke A.M. (2007). Identification and characterization of a Y-like primate retinal ganglion cell type. *J Neurosci* 27:1101911027.

[22] Pillow J.W., Shlens J., Paninski L., Sher A., Litke A.M., Chichilnisky E.J., & Simoncelli E.P. (2008). Spatio-temporal correlations and visual signalling in a complete neuronal population. *Nature* 454(7207):995-999.

[23] Trong P.K., & Rieke F. (2008). Origin of correlated activity between parasol retinal ganglion cells. *Nat Neurosci* 11(11):1343-1351.

[24] Völgyi B., Chheda S., & Bloomfield S.A. (2009). Tracer coupling patterns of the ganglion cell subtypes in the mouse retina. *J Comp Neurol* 512(5):664-687.

[25] Werblin F.S. (1972). Lateral interactions at inner plexiform layer of vertebrate retina: antagonistic responses to change. *Science* 175:10081010.

[26] Zaghloul K.A., Manookin M.B., Borghuis B.G., Boahen K., & Demb J.B. (2007). Functional circuitry for peripheral suppression in Mammalian Y-type retinal ganglion cells. *J Neurophysiol* 97:43274340.

This chapter presents the main material for the following manuscript:

Greschner, Martin; Heitman, Alexander K.; Field, Greg D.; Li, Peter H.; Ahn, Daniel; Sher, Alexander; Litke, Alan M.; Chichilnisky, E.J. "Recurrent suppression in ON parasol retinal ganglion cells".

The manuscript is in the final stage of preparation and will be submitted soon. The journal is still undecided. Dr. Martin Greschner is the primary researcher who did the majority of recordings, project formulation, and unconvered the key observation which anchors the manuscript. Alexander Heitman was the secondary researcher in charge of the modeling and simulation which led to two of the six figures. He also recorded some of the final pieces necessary for the pharmacological manipulations. Dr. Greg D. Field, Dr. Peter H. Li, and Mr. Daniel Ahn were all members of the collaborative lab and were instrumental in recordings and in formulating the project. Dr. Alexander Sher and Dr. Alan M. Litke developed the multi-electrode array which enables the unique high-fidelity population recordings necessary for undertaking this project. Finally Dr. EJ Chichilnisky is the PI of the lab where the research conducted. He and Dr. Martin Greschner were the main drivers of the project. The author is thankful to everyone for their contributions.